REVIEW

*National Science Open*
5: 20250049, 2026
https://doi.org/10.1360/nso/20250049

Materials Science

Special Topic: Intelligent Materials and Devices

# Advancements in hollow-core anti-resonant fiber for gas sensing applications

Jing Cheng[1,#], Hao Wang[1,2,#], Lei Zhang[2,*], Yonggang Huang[3], Peng Jiao[3], Haitao Guo[4], Yantao Xu[4], Yinsheng Xu[1,*] & Xianghua Zhang[1,5]

[1]*State Key Laboratory of Silicate Materials for Architectures, Wuhan University of Technology, Wuhan 430070, China;*
[2]*State Key Laboratory of Optical Fiber and Cable Manufacture Technology, Yangtze Optical Fibre and Cable Joint Stock Limited Company (YOFC), Wuhan 430073, China;*
[3]*Institute of Special Glass Fiber & Optoelectronic Functional Materials, China Building Materials Academy, Beijing 100024, China;*
[4]*State Key Laboratory of Transient Optics and Photonics, Xi'an Institute of Optics and Precision Mechanics, Chinese Academy of Sciences (CAS), Xi'an 710119, China;*
[5]*Institut des Sciences Chimiques de Rennes - UMR CNRS 6226, Universitéde Rennes, Rennes 35042, France*

#Contributed equally to this work.
*Corresponding authors (emails: zhanglei@yofc.com (Lei Zhang); xuyinsheng@whut.edu.cn (Yinsheng Xu))

Received 15 September 2025; Revised 30 October 2025; Accepted 31 October 2025; Published online 5 November 2025

**Abstract:** Hollow-core anti-resonant fibers (HC-ARFs) have emerged as a transformative platform for high-performance gas sensing. This review systematically summarizes recent advances in HC-ARF-based gas sensors. It begins by elucidating the light-guiding principles of HC-ARFs. Subsequently, key strategies for enhancing sensor performance are discussed, encompassing structural optimization of the fiber, selection of mid-infrared substrate materials, femtosecond laser fabrication of microchannels to accelerate gas diffusion, and surface modification with functional materials for improved selectivity. The core of the review analyzes representative sensing techniques integrated with HC-ARFs, including direct absorption spectroscopy (DAS) and its highly sensitive derivatives, photothermal and photoacoustic spectroscopy, as well as multiplexed Raman spectroscopy. Finally, current challenges and future prospects are outlined, highlighting the potential of HC-ARF sensors to achieve ultra-sensitive, rapid, and compact gas detection for various applications.

**Keywords:** HC-ARF, fiber optics, direct absorption spectroscopy, laser spectroscopy, gas sensing

## INTRODUCTION

Recent advances in specialty optical fiber fabrication have significantly transformed the field of gas sensing with hollow-core fibers (HCFs). Among these, hollow-core anti-resonant fibers (HC-ARFs) trap light within their low-refractive-index air cores through the combined effects of the anti-resonant reflecting optical waveguide (ARROW) mechanism and inhibited coupling (IC) theory, which reduces the impact of fiber material properties on transmission performance [1]. Compared to hollow-core photonic bandgap fibers

© The Author(s) 2025. Published by Science Press and EDP Sciences. This is an Open Access article distributed under the terms of the Creative Commons Attribution License (https://creativecommons.org/licenses/by/4.0), which permits unrestricted use, distribution, and reproduction in any medium, provided the original work is properly cited.

(HC-PBGFs), which guide light via the photonic bandgap effect, HC-ARFs do not require a periodic cladding structure and provide a wider transmission bandwidth [2,3]. Additionally, HC-ARFs have faster gas diffusion due to their larger core size and offer several key advantages, including low transmission loss, a large mode field area, and enhanced single-mode performance [4]. Using HC-ARFs as a medium for light-gas interaction allows efficient coupling between gas molecules and optical fields over long distances. Unlike free-space optical systems that utilize multipass cells (MPCs) to enhance light-gas interactions [5], HC-ARF-based gas sensors achieve higher sensitivity with smaller sample volumes, thereby supporting system miniaturization [6].

In this review, we systematically summarize recent progress in HC-ARF-based gas sensing. First, the light-guiding mechanism of HC-ARFs is briefly introduced. Second, strategies for enhancing the performance of HC-ARF gas sensors are discussed. Subsequently, the operating principles and characteristics of representative HC-ARF-based sensing techniques, including direct absorption spectroscopy (DAS) and its derivatives, as well as Raman spectroscopy (RS), are analyzed. Finally, current challenges and prospective directions in HC-ARF gas sensing are outlined to guide the development of high-performance fiber-optic gas sensors.

## LIGHT GUIDANCE PRINCIPLE OF HC-ARFS

In sharp contrast to the total internal reflection mechanism of solid-core fibers, the light-guiding principle of HC-ARFs primarily relies on the ARROW theory. The essence of this theory lies in the reflection and refraction of light at the interface between the hollow core and the cladding: part of the light is reflected into the core, while the remainder propagates into the cladding. After entering the cladding tubes, the refracted light undergoes multiple reflections between the inner and outer interfaces, forming stable multi-beam interference within the wavelength-scale thin cladding layers. This process essentially constitutes a Fabry-Pérot (F-P) resonant cavity [7,8].

When the incident wavelength satisfies the anti-resonant condition of the F-P cavity, the light is refracted back into the core, and the originally reflected light undergoes in-phase superposition, resulting in high reflectivity at the cladding interface. Consequently, optical energy is effectively confined within the hollow core for transmission, corresponding to the low-loss region in the transmission spectrum (yellow region in Figure 1a). Conversely, when the wavelength meets the resonant condition, the refracted light resonates within the cladding, causing the optical energy to leak through the cladding and leading to a sharp increase in transmission loss within the core. This corresponds to the high-loss peaks in the transmission spectrum (orange region) [9]. The mode simulation of the fundamental mode ($LP_{01}$) of HC-ARF under both resonant and anti-resonant conditions is illustrated in Figure 1b [10]. The anti-resonant wavelength is expressed by Eq. (1):

$$\lambda = \frac{2t\sqrt{n_1^2 - n_2^2}}{m - 0.5}, \tag{1}$$

where $n_1$ and $n_2$ denote the refractive indices (RI) of the cladding and core, respectively, $t$ represents the cladding thickness, $\lambda$ represents the anti-resonant wavelength, and $m$ is a positive integer corresponding to the anti-resonance order.

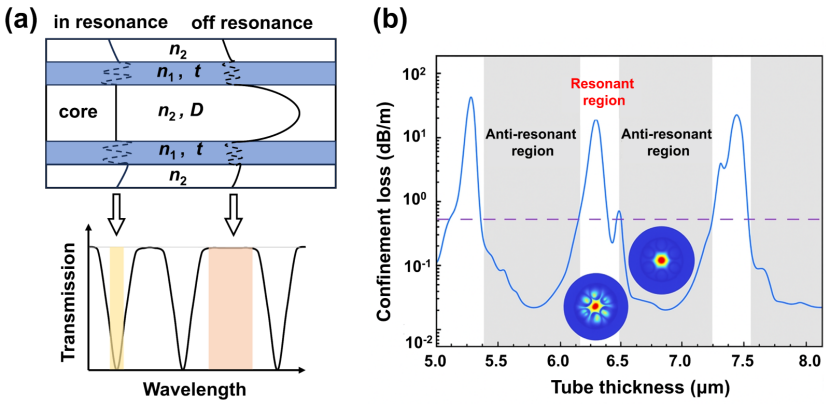


**Figure 1** (a) Illustration of the light-guiding principle in an HC-ARF (adapted from Ref. [9]). (b) Mode simulation of the $LP_{01}$ mode in the HC-ARF under resonant and anti-resonant conditions (adapted from Ref. [10]).

The ARROW theory elucidates the formation mechanism of discrete high-transmission bands in the optical transmission spectra of fibers. It demonstrates that both the spectral positions and bandwidths of these bands in HC-ARFs primarily depend on the capillary wall thickness, the RI of the air core, and the RI of the capillary wall material. This theory provides the fundamental framework for understanding the optical transmission characteristics of HC-ARFs.

In addition, because both the core and cladding tubes of an HC-ARF are filled with air and thus share the same RI, stable waveguide modes can exist in both regions when the anti-resonant condition is satisfied. When the effective RI of the core and cladding-tube modes approach each other, energy transfer between these modes occurs, leading to leakage of core-mode energy through the cladding and a consequent increase in optical loss. Figure 2 provides an intuitive illustration of the IC principle [11]. It can be observed that as the diameter of the cladding tube ring gradually increases, the effective RI of the cladding like-$LP_{01}$ mode also increases correspondingly. When the effective RI of the like-$LP_{01}$ mode in the cladding tube ring and the higher-order core mode ($LP_{11}$) coincide, mode coupling occurs, resulting in energy leakage of the higher-order mode. Furthermore, based on the variation trend of the effective RI of these modes, it is evident that if the tube-ring diameter is further increased, the like-$LP_{01}$ mode in the cladding tube ring strongly couples with the core $LP_{01}$ mode, leading to substantial optical loss.

Therefore, to minimize energy leakage from the core, the fiber design must simultaneously satisfy the anti-resonant condition and suppress coupling between the fundamental core mode and the cladding-tube modes. This can be achieved by optimizing the cladding tube configuration, such as reducing the capillary-to-core diameter ratio or incorporating nested structures, to increase the effective RI difference and mitigate mode-coupling loss. Conversely, selectively enhancing the coupling of higher-order core modes facilitates their leakage, thereby improving the fiber's single-mode performance.

## PERFORMANCE OPTIMIZATION OF HC-ARF GAS SENSORS

Fiber-optic gas sensors combine conventional spectroscopic techniques with optical fiber technology to

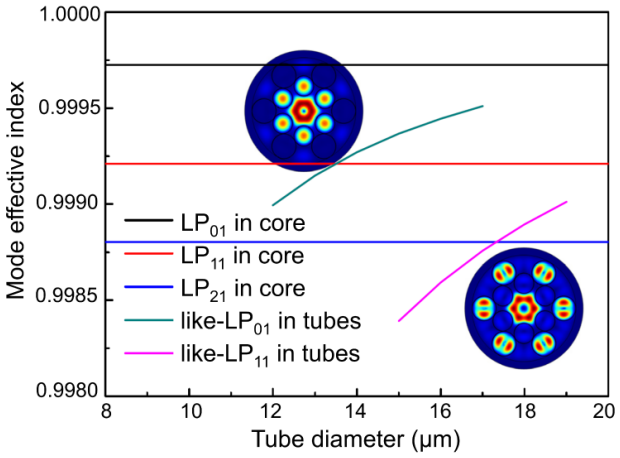


**Figure 2** The modal contents in core and tubes [11].

identify gas species and quantify their concentrations by monitoring variations in light properties, such as intensity, wavelength, frequency, phase, and polarization, induced by light-gas interactions. Key performance metrics for these sensors include sensitivity, limit of detection (LoD), and response time [12]. In practical applications, additional factors such as long-term stability, selectivity, and repeatability must also be considered [13]. Current research on HC-ARF-based gas sensors focuses on enhancing measurement accuracy, shortening response time, and enabling multi-gas detection. To achieve these goals, researchers have pursued performance improvements through structural optimization, material selection, microchannel fabrication, and surface modification.

## Structural optimization

Building on a comprehensive understanding of the light-guiding mechanism in HC-ARFs, researchers have achieved low-loss, single-mode transmission over a broad spectral range by refining the design and optimizing the structural parameters of the fiber.

Since the first HC-ARF was reported (Figure 3a) [14], numerous novel fiber structures have been designed and fabricated. In 2011, Wang *et al*. [15] identified the shape of the core's inner wall as the primary factor influencing transmission performance. By optimizing this geometry, an HCF with a hypocycloid-shaped inner wall, later termed the negative-curvature HCF, was fabricated in 2012, achieving record-low loss (Figure 3b) [16]. In the same year, the introduction of HC-ARFs featuring an ice-cream-cone-shaped cladding extended the transmission window from the visible to the mid-infrared (MIR) region (Figure 3c) [17]. However, in both designs, "Fano resonances" induced by junctions between cladding tubes increased transmission loss. Node-less HC-ARFs were subsequently developed to significantly reduce bending loss and broaden the transmission bandwidth (Figure 3d) [18]. In 2018, Gao *et al*. [19] successfully fabricated a conjoined-tube HC-ARF (Figure 3e). By precisely controlling parameters, they mitigated the adverse effects of coupling between cladding and core modes at the nodes, thereby reducing fiber loss. Subsequently, researchers discovered that incorporating nested structures increases the effective RI difference between the core fundamental mode and the cladding tube modes, which reduces mode coupling and enhances optical

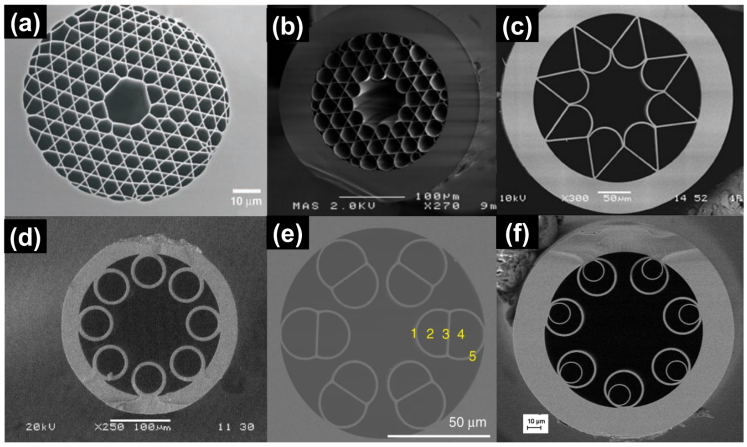


**Figure 3** Scanning electron microscopy (SEM) images of HC-ARFs. (a) The first Kagome type fiber [14]. (b) Negative curvature fiber [16]. (c) Ice-cream-cone HC-ARF [17]. (d) Node-less HC-ARF [18]. (e) Conjoined tube HC-ARF [19]. (f) Nested HC-ARF [21].

field confinement. HC-ARFs with nested structures exhibit broader transmission bandwidths, lower losses, and improved single-mode transmission performance (Figure 3f) [20,21].

Recently, advances in understanding the light-guiding mechanisms of HC-ARFs have promoted the diversification and functionalization of their structural designs. As illustrated in Figure 4, researchers have proposed various novel HC-ARF configurations that achieve substantial reductions in transmission loss across specific wavelength bands through optimized optical field confinement and mode control [22–29]. Some of these designs have demonstrated propagation losses on the order of dB $km^{-1}$. However, such low-loss fibers are currently employed mainly in applications with stringent loss requirements, such as high-power laser delivery and broadband optical communications. Moreover, as structural designs become increasingly sophisticated, existing fabrication techniques encounter growing challenges and limitations, thereby constraining further engineering applications and performance optimization.

## Substrate material selection

The MIR spectral region, spanning 2.5–13 μm, is of critical importance for gas sensing because many gas molecules exhibit strong ro-vibrational transitions within this range, leading to fundamental vibrational absorption bands. These fundamental absorption peaks are typically 2–3 orders of magnitude stronger than the corresponding overtone peaks in the near-infrared (NIR) region (0.75–2.5 μm). Consequently, extending the operating window of HC-ARFs into the MIR region enables more sensitive detection of a broader range of gases.

According to the light-guiding principle of HC-ARFs, one effective approach to reducing transmission loss in the MIR band is to optimize the geometric design of the fiber, thereby minimizing the overlap between the core mode field and the microstructured cladding. In 2023, Belardi's team [30] at the University of Lille shifted the transmission window toward longer wavelengths by increasing the fiber core diameter and the wall thickness of cladding quartz glass tubes, achieving a minimum loss of 0.22 dB $m^{-1}$ at 4.6 μm in an eight-tube single-ring HC-ARF. In 2024, Arman *et al*. [31] first optimized the cladding tube dimensions and core diameter of a seven-tube single-ring HC-ARF, reducing the confinement loss (CL) of the fiber to 3.5 ×

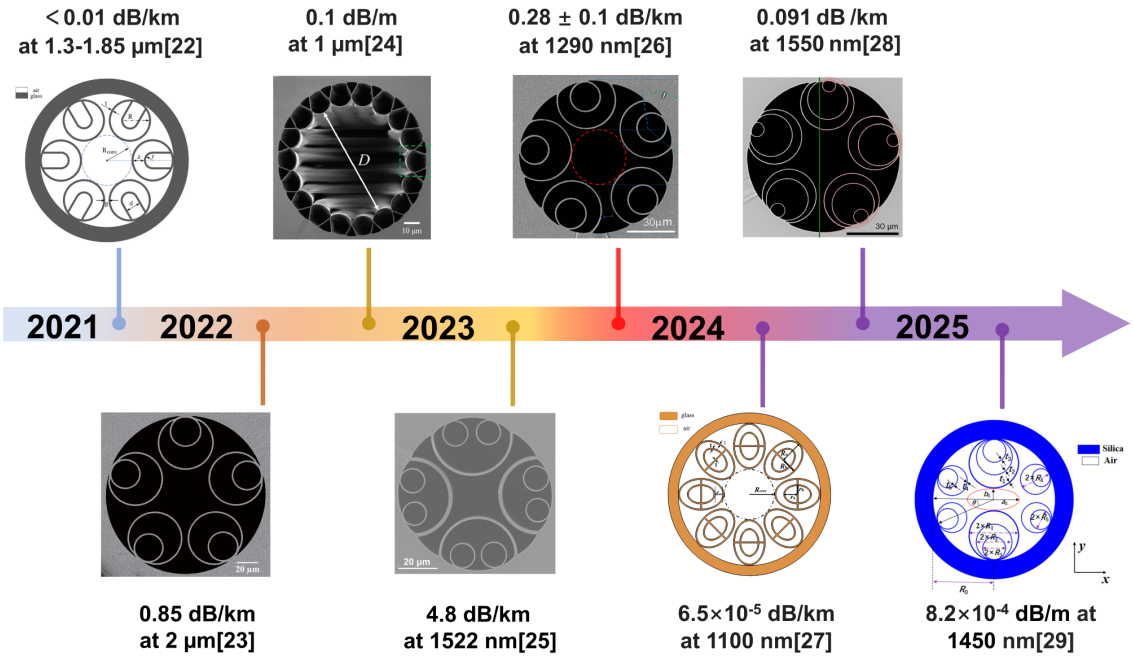


**Figure 4** Cross-sections of recently developed low-loss HC-ARFs [22–29].

$10^{-2}$ dB $m^{-1}$ at 3.3 μm. They subsequently introduced nested tubes within the cladding to construct a more efficient anti-resonant structure, aiming to further suppress leakage loss. Simulation results showed that the CL values of the secondary structure with nested elements and the tertiary structure with nested-in-nested rings were significantly lower than those of the original configuration, with respective losses of $3.5 \times 10^{-2}$, $4.76 \times 10^{-3}$, and $1.85 \times 10^{-4}$ dB $m^{-1}$. However, due to the intrinsic absorption of silica, further reducing transmission loss in the MIR band remains challenging, making it difficult to extend the operating wavelength beyond 4.5 μm [32].

Chalcogenide and tellurite glasses exhibit high transparency and broad transmission windows in the MIR band, thus enabling effective overcoming of the above limitations when used as the substrate materials. In 2024, Zhu *et al*. [33] designed and fabricated a tellurite-based HC-ARF that exhibits multiple low-loss transmission bands across the 3–6 μm range. Its theoretical loss in the anti-resonant bands could be reduced to 0.1 dB $m^{-1}$ through further structural optimization. In the following year, they optimized the fabrication process through precise pressure control, achieving a record-low loss of $0.3 \pm 0.02$ dB $m^{-1}$ at 4.65 μm and extending the transmission capability up to 10 μm [34]. In 2021, Yao *et al*. [35] reported a MIR absorption spectroscopy system based on a tellurite HC-ARF coupled with a quantum cascade laser (QCL), achieving highly sensitive NO detection at 5.26 μm. Additionally, several low-loss chalcogenide HC-ARFs have been developed for broadband MIR operation. He *et al*. [36] first designed and successfully fabricated a large-mode-area, all-solid chalcogenide anti-resonant fiber operating in the MIR spectral range of 4.5–7.5 μm, with a minimum loss of 7 dB $m^{-1}$ at 4.8 μm. Zhang *et al*. [37] later designed a seven-hole chalcogenide HC-ARF with touching cladding capillaries, fabricated from purified $As_{40}S_{60}$ glass using the "stack-and-draw" technique combined with dual gas-path pressure control, achieving a measured fiber loss as low as 1.29 dB $m^{-1}$ at 4.79 μm. Subsequently, by optimizing the fiber structure into a six-cell nodeless HC-ARF,

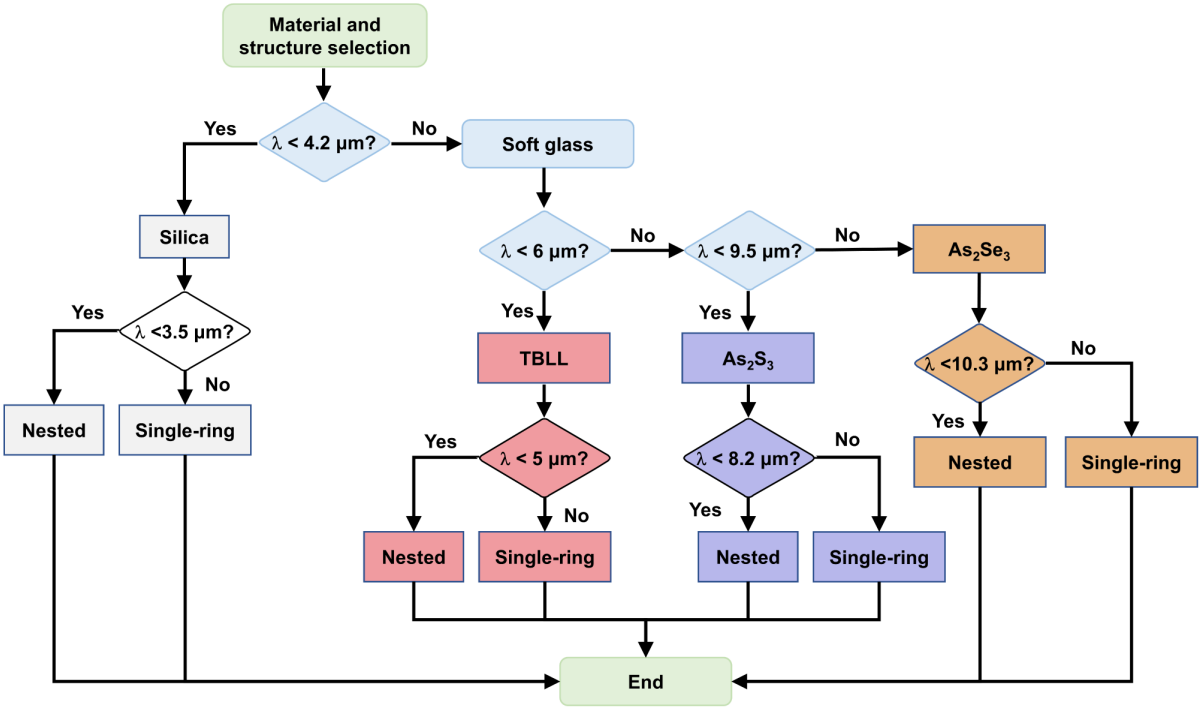


**Figure 5** Selection process of materials and cladding structures for HC-ARFs across different wavelength regions (adapted from Ref. [43]).

they further reduced the loss at 4.79 μm to 0.56 dB $m^{-1}$ [10]. However, tellurite fibers have difficulty operating beyond 6 μm due to phonon energy limitations [38]. In contrast, chalcogenide glasses exhibit excellent transparency across the 2–11 μm range, along with stable physicochemical properties and strong glass-forming ability, making them promising candidates for high-transmittance optical fibers in the long-wave infrared (LWIR) region [39]. In 2016, Gattass *et al*. [40] fabricated an HC-ARF from chalcogenide glass via extrusion molding, achieving a low-loss window spanning 9.5–11.5 μm in the LWIR region, with a minimum loss of 2.1 dB $m^{-1}$ at 10 μm. In a similar vein, Hayashi *et al*. [41] developed a chalcogenide glass-based HC-ARF, extending its operating wavelength to 11 μm. These advancements demonstrate the feasibility of gas sensing using HC-ARFs at ultra-long wavelengths. In 2023, Hu *et al*. [42] detected the strong absorption line of ethylene ($C_2H_4$) at 10.5 μm using a chalcogenide HC-ARF, highlighting its potential as a promising platform for MIR gas sensing.

It is worth noting that Zhang *et al*. [43] recently proposed an analytical framework for evaluating the total loss of single-ring and nested tubular HC-ARFs fabricated from silica, tellurite, and chalcogenide glasses. They systematically investigated the effects of RI, material absorption, and cladding structure on various loss mechanisms and presented a decision-making process for selecting fiber materials and cladding structures based on the operating wavelength, as shown in Figure 5. The results offer a comprehensive guideline for material selection and structural optimization to enhance the transmission performance of MIR HC-ARFs.

## Microstructural processing

According to the Beer-Lambert law, laser-based gas spectroscopy relies on the interaction path length

between light and target gas molecules. Therefore, increasing the optical path length is typically employed to enhance sensor sensitivity. However, due to core size constraints, depending solely on passive gas diffusion in HC-ARFs results in long gas-filling times for long fiber lengths. Although pressure-assisted filling significantly reduces the response time, it increases the complexity of the sensing device. The development of precision machining technology enables the fabrication of microchannels on optical fibers and offers novel approaches to improving the response time of HC-ARF-based sensors. Since optical fibers are brittle materials, non-contact processing methods such as femtosecond laser (FSL) or focused ion beam (FIB) can reduce mechanical damage and efficiently etch microchannel structures on the surface of fibers. FIB has the advantages of high precision, high resolution, and low damage, but the etching speed is exceedingly slow, and the effective processing range of FIB can be limited during high-precision processing [44,45]. With its ultra-narrow pulse width and extremely high peak intensity, FSL has become an important tool for the fabrication of optical fiber sensors with novel microstructures. By focusing the laser beam inside the material, the laser can trigger nonlinear interactions in the focusing region to fabricate specific microstructures. However, certain transmission loss occurs during the fabrication of microchannels by FSL, which is mainly attributed to local damage of the fiber structure or glass debris generated during the laser ablation process [46,47].

In 2021, Kozioł *et al*. [48] determined the optimal laser processing parameters by controlled experiments and processed 25 microchannels, with the process resulting in only a low transmission loss of 0.17 dB. In 2025, the same research team investigated the influence of microchannels on gas diffusion rates using a low-loss microchannel fabrication approach [49]. The results demonstrated that increasing the number of microchannels significantly accelerated gas diffusion, reducing the diffusion time from approximately 6 h to 330 s when all microchannels were fully opened. Further experiments with different inter-channel spacings (15, 31, and 62 cm) confirmed that shorter spacing markedly enhanced the diffusion rate. Moreover, the diffusion time was found to be independent of the total fiber length when the inter-channel spacing remained constant, underscoring the general applicability of the microchannel design. Similarly, Liu *et al*. [50] employed FSL processing to fabricate microholes in HCFs for barometric pressure sensing. Experimental results revealed that the response speed of the ten-hole sensor was approximately twice that of the single-hole sensor. This significant enhancement in response speed is attributed to the improved gas diffusion pathways provided by the FSL-fabricated microporous channels, which effectively enhance gas diffusion efficiency.

FSL microchannel fabrication has emerged as an effective method to improve the response speed of HC-ARF-based gas sensors [51–53]. Figure 6 shows scanning electron microscopy (SEM) images of microchannels fabricated in HC-ARFs using FSL [49,54–56]. However, the mechanisms by which microchannel size, geometry, and distribution influence optical attenuation remain to be systematically clarified. Furthermore, substantial opportunities exist to enhance structural fabrication quality, geometric precision, and process flexibility.

## Surface modification

With the advancement of nanotechnology, the design strategy of fiber-optic gas sensors has increasingly focused on functionalization using sensitive materials. Two-dimensional materials such as graphene, transition metal dichalcogenides, and black phosphorus can significantly enhance the adsorption capacity of gas

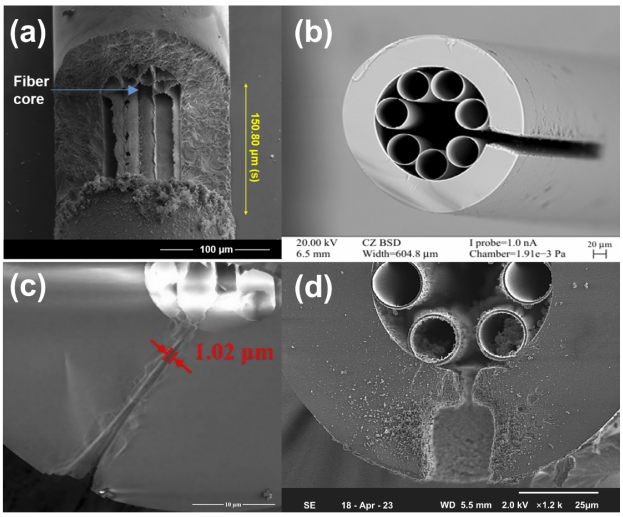


**Figure 6** SEM images of microchannels. (a) A slot machined on the fiber with material removed down to the bottom surface of the hollow core [54]. (b) SEM image of a single channel cross-section [49]. (c) The core diameter of the side-drilled microchannel on the fiber is approximately 1.02 µm near the hollow core region [55]. (d) SEM images of the cleaved end of the micro-drilled optical fiber [56].

molecules. When the functionalized coating interacts with a target gas, its properties change, resulting in a change in the output optical signal. This method of coating sensitive membranes has been successfully applied in evanescent wave fiber-optic gas sensors [57–61] and photonic crystal fiber (PCF)-based gas sensors [62,63]. However, within HC-ARFs, such functionalization has been primarily explored for biosensing applications [64–66], with relatively few studies focused on gas detection. In 2021, Liu *et al*. [67] demonstrated the *in situ* construction of a ZnO-$Bi_2O_3$ nanosheet heterojunction on the inner wall of an HC-ARF. By exploiting the RI variation induced by the interaction between the heterojunction and acetone molecules to modulate the optical signal, they achieved highly sensitive and selective acetone detection at room temperature, demonstrating the potential of this approach for early breath-diagnosis applications.

In addition, the surface plasmon resonance (SPR) effect can be introduced by modifying the microstructured fibers with metallic materials through filling or coating. SPR is a resonant optical coupling phenomenon occurring at the interface between a metal and a dielectric. When a beam of light is incident at this interface at a specific frequency and angle, it excites the free electrons on the metal surface to oscillate collectively, generating surface plasmons. When the plasmon exists at a specific frequency, it is called a surface plasmon wave (SPW). Resonant coupling occurs when the wave vectors of the external electromagnetic wave and the SPW match, which is the SPR effect [68]. Li *et al*. [69] first reported an HC-ARF methane ($CH_4$) sensor based on the SPR effect. As illustrated in Figure 7a, when light is incident at the interface between the core and the gold-coated antiresonant tubes, SPWs are excited, allowing part of the optical energy to couple into surface plasmon modes and produce a distinct attenuation peak (Figure 7b). The RI of the gas-sensitive layer covering the gold film decreases linearly with increasing $CH_4$ concentration, thereby modifying the phase-matching condition for SPR and resulting in a blue shift of the attenuation peak in the transmission spectrum (Figure 7c). By monitoring the resonant wavelength shift in real time with an optical spectrum analyzer (OSA), highly sensitive $CH_4$ detection was achieved, exhibiting a sensitivity of 5.54 nm·%$^{-1}$—superior to most reported optical fiber-based $CH_4$ sensors.

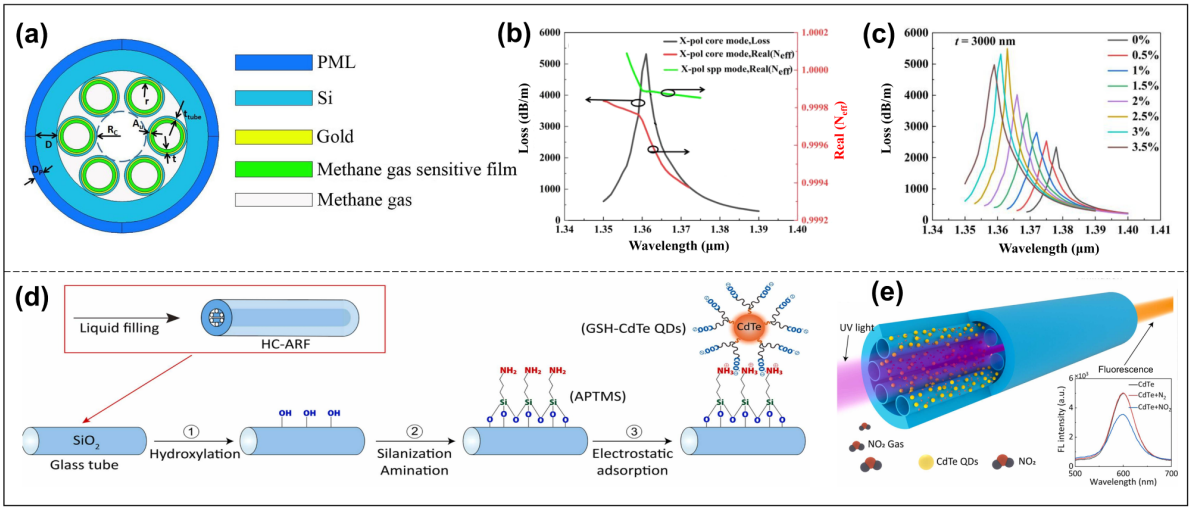


**Figure 7** Surface functionalization strategies for HC-ARFs. (a–c) SPR-based optical fiber $CH_4$ gas sensor [69]: (a) Cross-sectional of the HC-ARF; (b) X-pol core modes effective RI and loss spectrum; (c) the loss spectrum within the range of $CH_4$ concentration from 0 to 3.5%. (d, e) HC-ARF gas sensor functionalized with GSH-CdTe QDs [76]: (d) immobilization process of CdTe QDs inside the HC-ARF; (e) illustration of $NO_2$ gas-induced fluorescence quenching.

Furthermore, the SPR effect serves as a major contributor to the electromagnetic mechanism (EM), which, together with the chemical mechanism (CM), constitutes the enhancement mechanisms of surface-enhanced Raman spectroscopy (SERS) [70]. When molecules adsorb onto the surface of noble metal nanostructures, such as gold or silver, the localized surface plasmon resonance (LSPR) effect generates a strongly enhanced electromagnetic field in "hot spots," including nanogaps or sharp tips, which constitutes the primary source of SERS enhancement (EM). Additionally, chemical interactions such as charge transfer between the metal surface and the adsorbed molecules can alter the molecular polarizability, providing supplementary enhancement (CM) [71]. Compared with conventional Raman scattering, the SERS technique can enhance the Raman scattering cross-section of analytes by up to 15 orders of magnitude, and the Raman signal of target molecules can be intensified by several orders of magnitude [72]. The integration of SERS with HC-ARFs allows the hollow core to function as a microcavity for reaction and signal enhancement, where the extended interaction path length improves the reproducibility and reliability of SERS signals. Since the sample flows inside the fiber and interacts directly with both the light and the SERS substrate, this configuration is particularly suitable for *in situ* or online detection of fluid samples (gases or liquids). However, due to the low concentration of gas molecules and the limited contact area between analytes and nanoparticles, the SERS signal intensity is generally weak for gaseous species, and a mature optical fiber SERS-based gas detection strategy has not yet been established [73]. Consequently, most current applications remain focused on liquid-phase detection [66,74,75]. Notably, Gao *et al*. [76] proposed a novel approach for highly sensitive nitrogen dioxide ($NO_2$) detection by functionalizing an HC-ARF with quantum dots (QDs). They immobilized glutathione (GSH)-capped CdTe QDs on the inner surface of the fiber via a self-assembly process, as illustrated in Figure 7d, e. Leveraging the fluorescence-quenching effect of the QDs, the fluorescence intensity changes upon interaction between $NO_2$ molecules and the capped QDs. This sensor enables rapid and efficient detection of $NO_2$ at concentrations as low as 0.1 ppm, with a sampling time of only a few minutes, significantly faster than many non-fiber-optic systems.

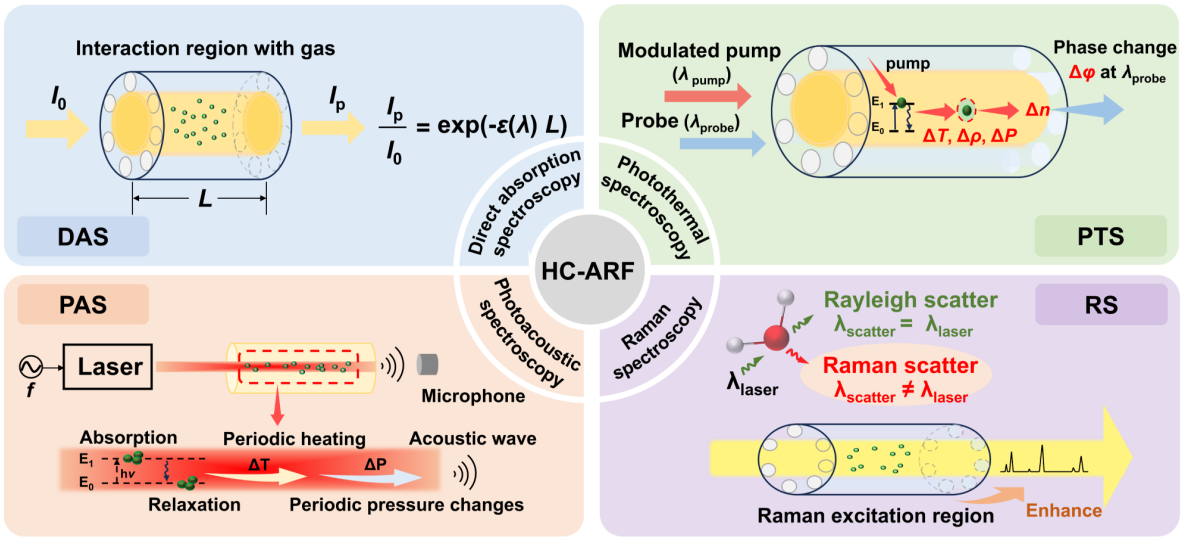


**Figure 8** Schematic of representative laser spectroscopy principles based on HC-ARFs.

Functionalization of HC-ARFs by selectively filling or coating functionalized materials into all or part of the air holes significantly improves the selectivity and sensitivity of the resulting gas sensors. This approach facilitates the development of sensors with high selectivity and high sensitivity. However, a major technical challenge lies in achieving a uniform and stable distribution of nanoparticles on the complex inner-wall geometry of HCFs. Currently, surface-modified HC-ARF gas sensors remain at an early developmental stage, and there is still substantial scope for further research.

## ADVANCES IN HC-ARF GAS SENSING RESEARCH

HC-ARFs can simultaneously serve as optical waveguides and micro-volume gas cells, providing an efficient platform for trace gas detection. As illustrated in Figure 8, based on the principle that light-gas interactions induce distinct optical effects, researchers have developed HC-ARF-based sensing platforms utilizing DAS, photothermal spectroscopy (PTS), photoacoustic spectroscopy (PAS), and RS for highly sensitive gas detection (Figure 8). On this basis, wavelength modulation spectroscopy (WMS) and frequency modulation spectroscopy (FMS) can be employed by applying wavelength modulation or frequency modulation to the pump laser, respectively. Utilizing these distinct principles and their corresponding modulation techniques, the sensors can achieve high sensitivity, good interference resistance, and long-term stability, offering excellent solutions for trace gas sensing in practical applications.

### Direct absorption spectroscopy and its derivative techniques

Laser absorption spectroscopy (LAS) is one of the most widely used techniques in laser-based gas sensing, with applications across industrial, environmental, and biomedical fields. This method is governed by the Beer-Lambert law (Eq. (2)), which states that selective absorption of laser light at specific wavelengths by

target gas molecules causes attenuation of the transmitted light intensity [12]. Among LAS techniques, tunable diode laser absorption spectroscopy (TDLAS) is particularly prominent, offering highly sensitive and selective gas detection with a relatively simple and cost-effective optical configuration [77]. However, because this approach relies on measuring the difference between incident and transmitted light intensities, the sensor's performance and accuracy are inherently limited. To address this limitation, PTS and PAS, which employ indirect detection mechanisms, have gained increasing research interest. Instead of directly measuring light intensity, PTS and PAS detect the thermal or acoustic responses generated by the absorption of light energy by gas molecules, thereby achieving high-sensitivity detection with an almost zero background [78]. Substantial progress has been achieved in developing HC-ARF-based gas sensors that integrate TDLAS, PTS, and PAS techniques.

$$\frac{I_{\mathrm{p}}}{I_0} = \exp(-\varepsilon(\lambda)L), \tag{2}$$

where $I_{\mathrm{p}}$ is the light intensity after passing through the gas sample, $I_0$ is the incident light intensity, $\varepsilon$ is the absorption coefficient of the gas, $\lambda$ is the wavelength of the light expressed in wavenumber, and $L$ is the light-gas interaction path length.

### *Tunable diode laser absorption spectroscopy*

TDLAS is a highly sensitive and straightforward laser spectroscopic technique derived from DAS. By tuning the diode laser's temperature or current to vary its wavelength, the laser scans across an absorption line of the target molecule. The resulting absorption of light produces an absorption spectrum signal proportional to the absorption intensity, enabling the measurement of relevant gas parameters [79,80].

DAS can be implemented using a simple setup consisting of a laser, an optical fiber, and a photodetector (PD). It enables a simple and intuitive visualization of the "fingerprint" of gas molecules, i.e., their characteristic absorption spectrum. Increasing the optical path length for light-gas interaction significantly improves the sensor sensitivity. HC-ARF is capable of achieving strong optical confinement, providing a viable approach to achieving a compact and stable long optical path. As shown in Figure 9a, Chai *et al*. [81] developed an all-fiber gas sensor that, by using a 5-m-long HC-ARF and a distributed feedback (DFB) laser centered at 2004.3 nm, along with a T-shaped three-way valve for gas filling and optical coupling, achieved a lowest LoD at the ppb level.

Additionally, sensor accuracy can be further enhanced by selecting MIR spectral bands with stronger absorption line intensities. Utilizing a tunable DFB MIR interband cascade laser (ICL) operating at one of the strongest absorption transitions of methane (3057.71 $\mathrm{cm}^{-1}$), Gomółka *et al*. [82] achieved ppb-level highly efficient methane detection. However, the light intensity signal in DAS is vulnerable to low-frequency noise interference, degrading the acquired absorption spectrum quality and restricting detection sensitivity. The modulation spectroscopy technique, developed by combining modulation techniques with tunable lasers, is able to suppress noise and improve the sensor performance.

WMS employs low-frequency laser scanning with a superimposed high-frequency sinusoidal modulation at a frequency of $f$. Using a lock-in amplifier, the second-harmonic ($2f$) signal is extracted from the absorption spectrum. This $2f$ signal is approximately proportional to gas concentration, enabling the determination of the target gas concentration. By shifting the absorption signal to a high-frequency region, WMS effectively

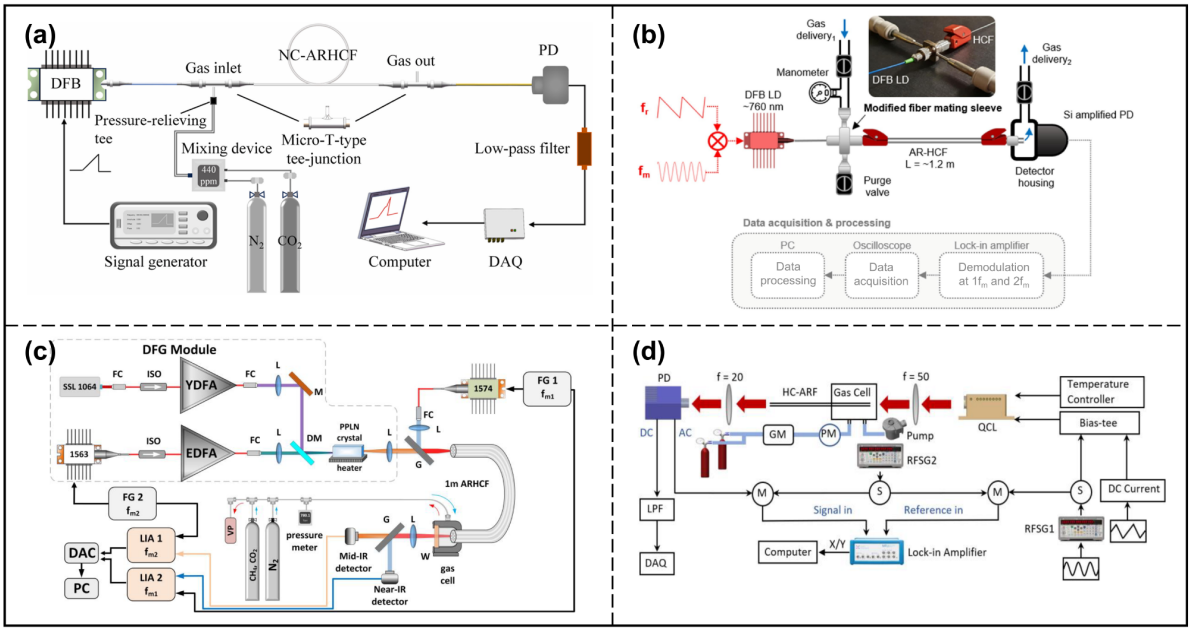


**Figure 9** HC-ARF gas sensors based on TDLAS. (a) DAS-based $CO_2$ sensor [81]. (b) WMS-based $O_2$ sensor [84]. (c) WMS-based dual-gas sensor for $CO_2$ and $CH_4$ [2]. (d) FMS-based NO sensor [86].

suppresses the impact of low-frequency noise, thereby enhancing the signal-to-noise ratio (SNR) of the system [83]. This was demonstrated in the work of Gomółka *et al*. [84] on an HC-ARF-based oxygen ($O_2$) sensor. As illustrated in Figure 9b, the experimental setup employed a DFB laser diode modulated by a sinusoidal wave at a frequency of $f_m$ = 1 kHz, with its 2*f* signal extracted using a lock-in amplifier. The study revealed that DAS struggled to distinguish weak signals from the fluctuating baseline when measuring broad absorption lines. In contrast, by optimizing parameters such as modulation depth in WMS, a remarkable LoD of 170 ppm was ultimately achieved, significantly enhancing the sensor performance. In 2020, Jaworski *et al*. [2] leveraged broadband and low-loss HC-ARFs combined with WMS technology to achieve dual-band gas detection in the NIR and MIR regions. As shown in Figure 9c, a 1.574 μm DFB laser and a 3.334 μm difference frequency generation (DFG) source were employed as excitation sources, corresponding to the characteristic absorption spectra of $CO_2$ and $CH_4$, respectively. Using a 1 m-long fused-silica HC-ARF with an 84 μm core diameter as the gas cell, the sensor achieved minimum LoDs of 24 ppb for $CH_4$ and 144 ppm for $CO_2$.

In WMS, a high-frequency sinusoidal modulation is applied to the laser injection current, enabling small-amplitude periodic wavelength scanning near the center of the absorption line, with modulation frequencies typically ranging from several kHz to tens of kHz. In contrast, FMS primarily employs direct current modulation or external electro-optic modulators (EOMs) to impose phase modulation on the laser at frequencies spanning from hundreds of MHz to GHz. Benefiting from its extremely high modulation frequency, FMS effectively suppresses low-frequency noise, pushing the system noise to the shot-noise limit and thereby significantly enhancing detection sensitivity [85]. Hu *et al*. [86] utilized a 35-cm-long tellurite HC-ARF for FMS detection of NO. The experimental setup is shown in Figure 9d, where a continuous-wave QCL served as the light source. The laser current was directly modulated by a radio frequency (RF) signal

generator to achieve frequency modulation in the range of 100–350 MHz. The RF output signal from the detector was subsequently down-converted to 200 kHz through signal mixing. The amplitude of the in-phase FMS-1*f* signal was then obtained by adjusting the relative phase difference between the input signal and the reference signal fed into the lock-in amplifier. The sensor exhibited a linear response within the concentration range of 0–100 ppm. Under a modulation depth of 13 dBm and a modulation frequency of 250 MHz, the noise-equivalent concentration (NEC) of the sensor reached 67 ppb, representing a 22-fold improvement over DAS.

However, amplitude-based signal extraction methods are highly sensitive to parasitic fluctuations in light intensity, and neither WMS nor FMS can fully eliminate additional optical signal variations caused by non-gaseous absorption effects (e.g., higher-order mode interference, structural non-uniformities, and environmental perturbations) [87–89]. Therefore, further enhancement of HC-ARF-based sensor performance requires not only optimization of the fiber structure but also improvement of the gas sensing methodology.

### *Photothermal spectroscopy*

PTS is a derivative of LAS that has the potential to achieve higher sensitivity over conventional TDLAS. Unlike DAS, PTS does not directly measure transmission spectrum changes, but rather detects thermal effects induced by gas light absorption. PTS systems employ a pump-probe dual-light configuration: A laser modulated by a specific-frequency sine wave generates pump light at a target wavelength, and when this pump light couples into an HC-ARF containing the target gas, the gas molecules undergo non-radiative relaxation, altering temperature, pressure, density, and other parameters inside the gas cell [90]. The resultant temperature variations induce periodic RI fluctuations in the target gas, described by Eq. (3) [91]:

$$\Delta n = \frac{(n-1)\varepsilon P_{\mathrm{exc}}}{T_0 4\pi\alpha^2 \rho C_{\mathrm{p}} f}, \tag{3}$$

where $n$ and $\varepsilon$ are the RI and absorption coefficient of the gas sample, respectively, $P_{\mathrm{exc}}$ is the pump power, $T_0$ is the absolute temperature, $\rho$ is the gas density, $C_{\mathrm{p}}$ is the specific heat at constant pressure, and $f$ is the pump modulation frequency. The change of $\Delta n$ in the RI induces a phase shift in the probe light (Eq. (4)) [92]:

$$\Delta\varphi = \frac{2\pi L \Delta n}{\lambda}, \tag{4}$$

where $L$ denotes the gas-light interaction path length, and $\lambda$ is the probe wavelength. Gas concentration retrieval is achieved by measuring the phase shift of the probe light. To prevent interference with the pump-target gas interaction, the probe wavelength is typically detuned from the target gas absorption line center. This approach enables the use of mature communication components, eliminating the need for expensive MIR detectors required in conventional schemes.

HC-ARF-based PTS enables efficient pump-probe-gas interactions within the hollow core. This configuration substantially reduces system volume and enhances operational stability while achieving high excitation and detection efficiencies. Due to the minute RI changes ($\Delta n \sim 10^{-9}$) induced by photothermal effects, most PTS gas sensors employ interferometric architectures to achieve high-sensitivity detection. To date, PTS-based trace gas sensing systems employing various interferometers, such as the Mach-Zehnder interferometer (MZI), Fabry-Pérot interferometer (FPI), and dual-mode fiber interferometer, have been successfully demonstrated.

MZI operates on two-beam interference principles. The probe light is split into a gas-exposed sensing arm and a noise-compensating reference arm. The photothermal effect causes a change in the RI within the sensing region to alter the optical path difference and phase difference between the arms. Gas concentration is retrieved by analyzing the change in the interference signal after beam recombination. In 2019, Yao *et al*. [93] demonstrated the first HC-ARF-assisted PTS sensor for CO detection. This system employed a typical active homodyne MZI configuration, in which the interferometer was locked at its quadrature point by winding a piezoelectric transducer (PZT) around the reference arm fiber and incorporating a feedback servo loop. However, this active phase-stabilization scheme not only introduced mechanical vibration noise from the PZT but also made the system highly susceptible to environmental disturbances, resulting in potential lock loss and increased complexity. To mitigate these issues, the team developed a heterodyne interferometry-based PTS technique in 2021 [94], eliminating the need for active stabilization in conventional MZIs. As illustrated in Figure 10a, the core innovation involved using an acousto-optic modulator (AOM) to introduce a 70 MHz frequency shift in the reference optical path, generating a heterodyne beat note between the sensing and reference beams at the PD. The phase variation induced by the photothermal effect was directly encoded in the phase of this beat signal and extracted through cascaded demodulation using a two-stage lock-in amplifier. This demodulation mechanism provided inherent immunity to probe laser power fluctuations. Experimental results confirmed that the photothermal signal amplitude remained stable even when the optical power in the sensing arm was attenuated by nearly 30 dB. For nitrous oxide ($N_2O$) detection using a 3.6 μm pump laser, this scheme achieved a normalized noise-equivalent absorption (NNEA) coefficient of $7.7 \times 10^{-9}$ $cm^{-1}$ W $Hz^{-1/2}$ within a 120-cm-long HC-ARF.

In contrast to MZI-based PTS sensors, FPI-PTS sensors feature a simpler design, in which two parallel highly reflective mirrors form a fixed-length cavity based on multiple-beam interference. When gas samples within the cavity undergo photothermal excitation, the resulting variations in RI modulate the phase of the resonating probe light. Typically, an HC-ARF-based FPI-PTS sensor sandwiches the HC-ARF between solid-core single-mode fibers (SMFs) to form an FPI (SMF-FPI) [95]. However, the small mode-field diameter of SMFs often causes a mismatch with that of HC-ARFs, resulting in significant optical loss. To address this issue, Yao *et al*. [96] improved the design by splicing the HC-ARF between a thermally expanded core (TEC) fiber and an indium fluoride ($InF_3$) multimode fiber (MMF) to construct a low-finesse F-P cavity, where the flat end faces of the solid-core fibers serve as cavity mirrors (Figure 10b). In this configuration, the mode-field diameter of the TEC fiber is enlarged through thermal expansion, while the MMF naturally possesses a sufficiently large mode-field diameter, effectively minimizing optical loss caused by mode-field mismatch. Compared with the SMF-FPI, this configuration increased the pump optical power inside the HC-ARF by a factor of 6.7. Potential interference resulting from the MMF's broadband transmission and multimode characteristics was mitigated using optical filters and precise coupling alignment. The experimental setup for gas sensing is illustrated in Figure 10c. The probe wavelength was actively stabilized at the quadrature point of the interferometer via a feedback control loop. Simultaneously, the injection current of the pump laser was scanned at 0.1 Hz and modulated with a sinusoidal waveform at frequency *f*. The output signal from photodetector (PD2) was demodulated at frequency *f* using a lock-in amplifier to obtain the first harmonic of the photothermal interference signal (PTI-1*f*). Experimental results demonstrated that water vapor accelerates the vibrational-translational relaxation of specific molecules, significantly enhancing the amplitude of the photothermal signal [93]. Consequently, the sample gas was

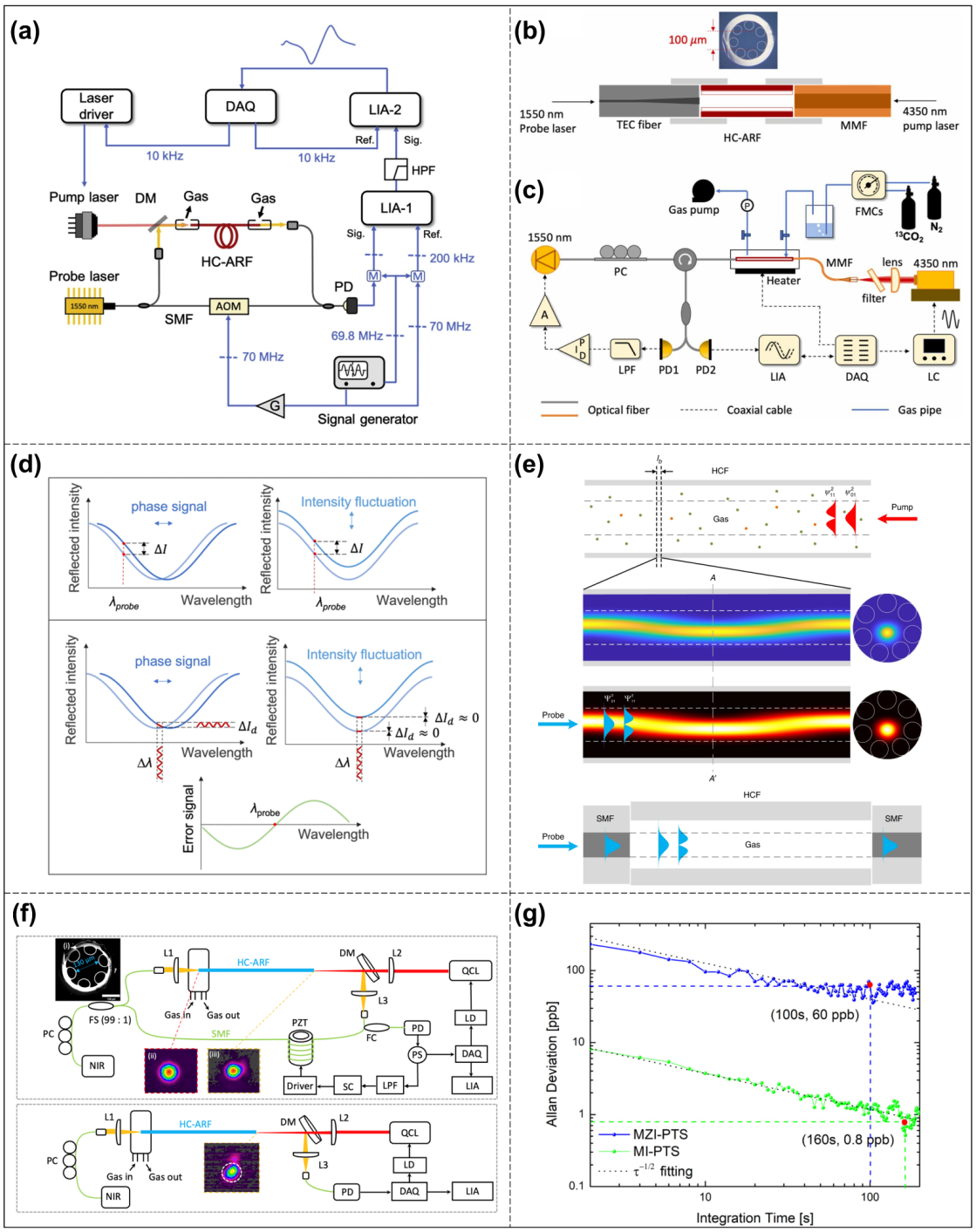


**Figure 10** HC-ARF gas sensors based on PTS. (a) Experimental setup of a heterodyne interferometric MZI-PTS gas sensor based on a HC-ARF [94]. (b, c) FPI-PTS-based $^{13}CO_2$ gas sensor [96]: (b) schematic of the F-P cavity; (c) schematic of the experimental setup. (d) Comparison of two FPI sensing processes: top, at the quadrature point; bottom, at the resonance point with wavelength dither [98]. (e) Schematic of the MPD-PTS principle [51]. (f, g) Comparative experiment on the sensing performance of MZI-PTS and MIPTS [100]: (f) experimental setups of (top) MZI-PTS and (bottom) MI-PTS; (g) Allan-Werle deviation as a function of integration time for both MZI-PTS and MI-PTS.

humidified to 100% relative humidity to improve sensor sensitivity. With an integration time of 23 s, the LOD for $^{13}CO_2$ reached 1 ppb. Extending the integration time to 240 s further reduced the LOD to 0.4 ppb, corresponding to a NEA of $1.4 \times 10^{-7}$ cm$^{-1}$. In 2025, Jiang *et al*. [97] developed an all-fiber F-P cavity configuration employing fiber Bragg gratings (FBGs) as cavity mirrors, leveraging their high reflectivity at specific wavelengths. The HC-ARF was mechanically spliced to two FBGs via a TEC adapter, with the fiber end faces angled at 8° to suppress unwanted reflections. This design enhanced both the finesse of the F-P cavity and the phase-to-intensity conversion efficiency of the probe light. Compared with the conventional SMF-FPI, the 1*f* photothermal signal amplitude increased fourfold. For $CH_4$ detection, this sensor achieved a NEC of 0.7 ppm with an integration time of 100 s.

Furthermore, improving signal demodulation techniques represents another critical pathway for enhancing the SNR and stability of PTS systems. Yao *et al*. [98] departed from the conventional method of locking the probe laser at the quadrature point of the interferometer and introduced a laser wavelength dithering (LWD) locking technique. In this method, the laser frequency is locked to a resonance peak of the FPI while a high-frequency sinusoidal dither is applied for fine modulation. The principle of error signal demodulation is illustrated in Figure 10d, where the photothermal signal is extracted by demodulating the FPI output at the dither frequency. By combining high-frequency modulation with narrowband detection, this technique effectively distinguishes genuine phase signals from low-frequency intensity fluctuations and external disturbances, thereby providing the sensor with excellent interference immunity. In $CH_4$ sensing experiments, this approach achieved a NNEA coefficient as low as $7.5 \times 10^{-9}$ cm$^{-1}$ W Hz$^{-1/2}$. These sensors clearly demonstrate the advantages of integrating HC-ARFs with photothermal interferometry, enabling zero-background measurements and enhanced sensitivity within a shortened optical path, and serve as a valuable reference for the development of compact, stable, and highly sensitive MIR gas sensors [99].

Mode-interferometer-based photothermal spectroscopy (MI-PTS) is a recently developed gas sensing technique distinguished by its high stability. This method, first proposed and demonstrated by Zhao *et al*. [51] in 2020, is referred to as mode-phase-difference photothermal spectroscopy (MPD-PTS). Its operating principle relies on detecting the phase difference between distinct guided modes ($LP_{01}$ and $LP_{11}$) in an HC-ARF. As illustrated in Figure 10e, when the pump light is absorbed by the target gas, the resulting localized temperature rise and RI variation induce photo-induced phase modulation in the co-propagating probe light. Because the $LP_{01}$ and $LP_{11}$ modes exhibit distinct field distributions, they experience different phase shifts, allowing gas concentration to be determined from the measured phase difference between the two modes. The MPD-PTS technique effectively suppresses common-mode interference from external perturbations such as temperature and pressure, significantly enhances the SNR, and maintains a linear relationship between the detected PTS signal and gas concentration. Experimental results demonstrate that this method achieves a sub-ppt detection limit for acetylene at NIR wavelengths (1532 nm), along with a wide dynamic range and excellent long-term stability. In 2025, Hu *et al*. [100] conducted a comprehensive investigation of this technique. Under identical experimental conditions, they systematically compared an actively servo-controlled MZI-PTS with a passively stabilized MI-PTS, as illustrated in Figure 10f. The results clearly demonstrated the superior performance of MI-PTS in both sensitivity and long-term stability. For NO detection, the MI-PTS system achieved a NEC of 0.8 ppb, compared with 60 ppb for MZI-PTS, representing a 75-fold enhancement in sensitivity. Furthermore, the NNEA of MI-PTS was two orders of magnitude better than that of MZI-PTS (Figure 10g). This remarkable performance difference primarily arises from the

outstanding common-mode noise rejection capability of MI-PTS, which results in a much lower noise floor than that of MZI-PTS, the latter being more susceptible to environmental phase and electronic feedback noise. In addition, the fully fiber-integrated interferometric architecture of MI-PTS eliminates the need for complex optical beam splitters and active feedback systems, greatly improving integration and robustness. In summary, by ingeniously combining high sensitivity and stability through a differential measurement mechanism, MI-PTS represents a highly promising pathway toward the development of next-generation compact trace gas sensors.

### *Photoacoustic spectroscopy*

The principle of PAS is analogous to that of PTS: absorption of pump light induces collisional relaxation in gas molecules, leading to periodic local pressure fluctuations that generate acoustic waves at the pump light's modulation frequency [101]. In PAS, the photoacoustic effect is typically amplified using an enlarged resonant cell or a multi-pass cavity. The amplitude of the generated acoustic waves, detected by microphones such as quartz tuning forks (QTFs), cantilever beams, or fiber-optic microphones, correlates directly with the gas concentration. The measured photoacoustic signal amplitude is given by Eq. (5):

$$S = S_{\mathrm{m}} P_{\mathrm{l}} c F \alpha + N, \tag{5}$$

where $S_{\mathrm{m}}$ is the microphone sensitivity, $P_{\mathrm{l}}$ is the pump optical power, $F$ is the cell-specific constant, $\alpha$ is the absorption coefficient of the gas, $c$ is the target gas concentration, and $N$ represents system noise. In PAS-based gas detection systems, acoustic signals generated by gas-light interactions are measured instead of optical signals. Consequently, detectors for photoacoustic spectra exhibit no wavelength dependence, are immune to scattered light effects, and feature a relatively simple system structure with high sensitivity.

In 2021, Zhao *et al*. [102] demonstrated a gas sensing platform based on photoacoustic Brillouin spectroscopy (PABS) by integrating PAS with HC-ARF gas sensing. As illustrated in Figure 11a, the HC-ARF simultaneously functions as a compact gas cell for pump light absorption and acoustic wave generation, an acoustic resonator, and an acoustic detector. Gas molecules inside the fiber core absorb the pump light, generating thermally induced acoustic waves that are resonantly amplified within the HC-ARF. Probe light from an external cavity diode laser (ECDL) is co-launched with the pump light into the gas-filled HC-ARF. Using a lateral-offset coupling technique, both $LP_{01}$ and $LP_{11}$ modes are excited in the HC-ARF, forming a dual-mode interferometer at the output SMF for detecting photoacoustically induced phase changes in the probe light. Experimental results demonstrate a LoD of 8 ppb for $C_2H_2$ with a 100 s integration time. Unlike conventional PAS, this PABS configuration eliminates the need for external microphones, thereby avoiding microphone-induced acoustic mode interference and enabling a more compact and stable system. Moreover, the differential phase detection approach effectively suppresses noise, significantly enhancing the system's immunity to environmental disturbances.

Building upon the elucidated mechanism of acoustic resonance enhancement in HC-ARFs, Xu *et al*. [103] pioneered the direct utilization of HC-ARF as a flexible acoustic resonator (Figure 11b). This cavity maintains a stable acoustic field distribution under various bending conditions (Figure 11c), establishing a novel pathway for developing compact and flexible PAS sensors suitable for complex scenarios. Concurrently, the role of HC-ARF in PAS systems has expanded beyond mere sensing elements to encompass

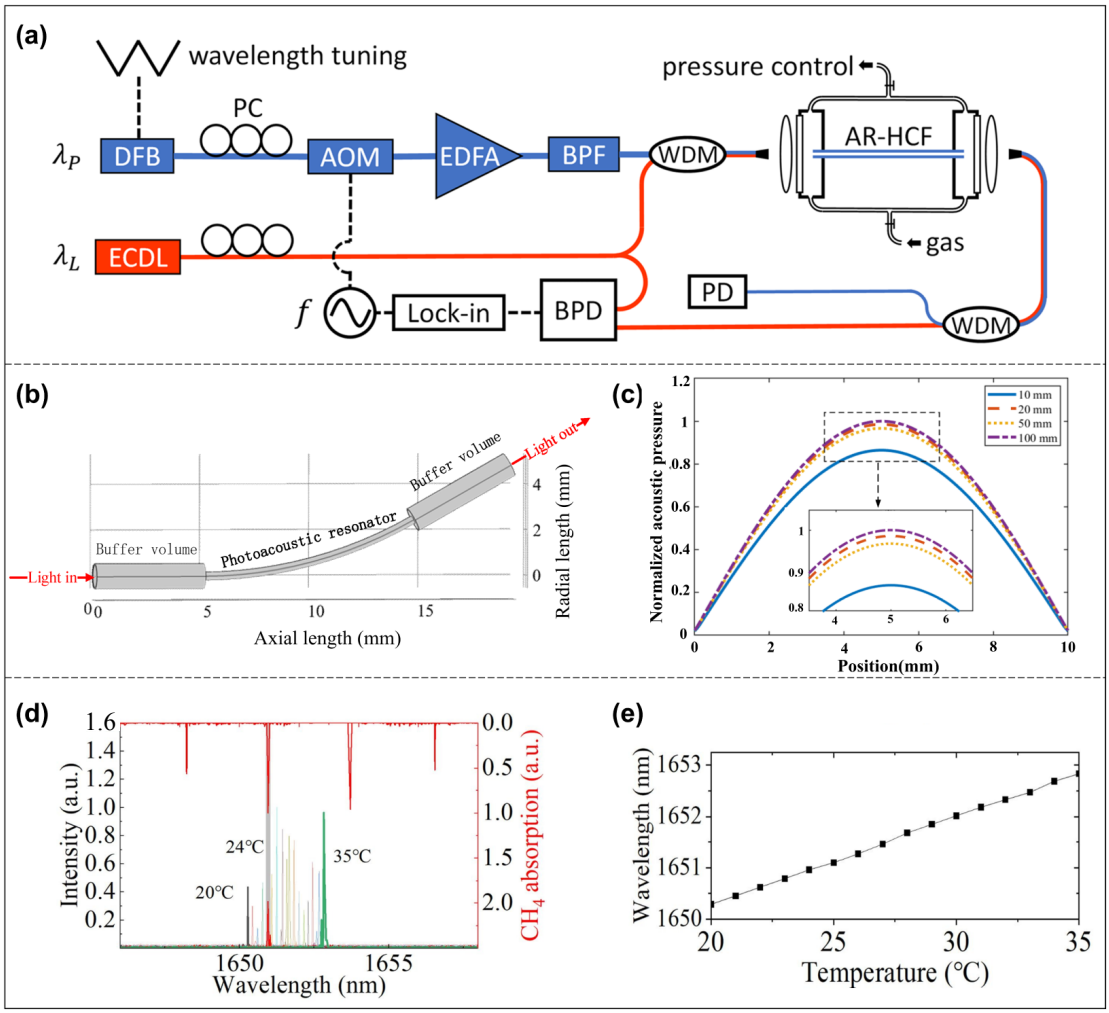


**Figure 11** Applications of HC-ARFs in PAS for gas sensing. (a) Experimental setup of the HC-ARF-based PABS system [102]. (b, c) Flexible longitudinal photoacoustic resonator based on HC-ARF [103]: (b) schematic structure of the resonator; (c) normalized acoustic pressure of the second-order eigenmode inside the resonator under different bending radii. (d, e) $H_2$-filled HC-ARF used as a PAS excitation light source [104]: (d) absorption spectrum of $CH_4$ and laser spectra around 1650 nm at different laser temperatures; (e) central wavelength of the sixth-order Stokes line as a function of laser temperature.

core light sources. Recently, Zhang *et al*. [104] employed a frequency comb-like Raman laser generated from a hydrogen ($H_2$)-filled HC-ARF as the excitation source for PAS detection of $CH_4$. The sixth-order rotational Stokes line at 1650 nm exhibited desirable characteristics of high pulse energy and narrow linewidth. As shown in Figure 11d, e, the precise tunability of this light source ensures optimal matching with $CH_4$ absorption lines, ultimately achieving an exceptional detection limit of 550 ppb.

However, the narrow core of HCFs results in considerable acoustic energy loss. Combined with the difficulties of integrating miniature microphones and the susceptibility of the sensing system to environmental noise [105], PAS has seen limited application in HCF-based gas sensing and remains at an early exploratory stage. Nevertheless, the aforementioned pioneering studies have established a feasible developmental pathway that will continue to drive HC-ARF-based PAS technology toward high-performance gas

sensing.

## Raman spectroscopy

Although techniques such as TDLAS, PTS, and PAS enable high-sensitivity gas detection, they require lasers operating at specific wavelengths for different target gases and are incapable of detecting homonuclear diatomic molecules. RS is a gas detection technique based on the Raman scattering effect. By measuring Raman scattered light from laser-excited samples, this technique determines molecular composition and concentration. Since RS directly reflects molecular vibrational and rotational structures, it enables the detection of all molecular gases except monatomic species. The principal advantage of RS lies in its capability to simultaneously detect multiple gas components using a single excitation wavelength, while offering stable, repeatable, non-destructive, non-contact, and non-consumptive measurements. However, because gases exhibit inherently small Raman scattering cross sections, the resulting Raman signals are typically weak with low peak intensities, which limits the practical application of RS in gas sensing [106]. The Raman signal intensity can be expressed by Eq. (6):

$$P \propto m\sigma V I_0, \tag{6}$$

where $P$ is the Raman signal intensity, $m$ is the molecular density, $\sigma$ is the Raman scattering cross section, $V$ is the volume of light-matter interaction, and $I_0$ is the laser power. According to the formula, Raman signal intensity can be significantly enhanced by increasing the gas molecular density, increasing the Raman scattering cross section, enlarging the light-matter interaction volume, and utilizing higher laser power.

Currently, the main approaches for enhancing Raman signals include cavity-enhanced Raman spectroscopy (CERS) [107], SERS [108], and fiber-enhanced Raman spectroscopy (FERS) [109]. Both CERS and SERS provide Raman signal enhancements of several orders of magnitude compared with conventional Raman scattering. However, these methods typically require large sample volumes and exhibit significant spectral interference, rendering them unsuitable for reusable or real-time online monitoring systems. In contrast, FERS has emerged as a promising technique for multicomponent gas analysis, employing HCFs as micro-volume gas cells. This configuration substantially increases the effective laser-gas interaction length and enhances the collection efficiency of Raman-scattered photons [110]. Furthermore, FERS requires only tens of microliters of sample gas, demonstrating strong potential for trace gas detection applications.

Buric *et al*. [111] established the foundational framework for HC-PBGF-based Raman gas sensing systems. Their setup employed transmission-based detection with commercially available low-loss ($< 0.4$ dB m$^{-1}$) HC-PBGFs, achieving a Stokes signal power enhancement of several hundred-fold compared with conventional free-space systems. However, during long-term, low-concentration multicomponent gas detection using HC-PBGFs, sensing performance is significantly degraded by the silica Raman background. Unlike HC-PBGFs, HC-ARFs exhibit reduced spatial overlap between the core mode and the cladding structure, resulting in lower susceptibility to silica Raman interference.

In 2023, Wan *et al*. [112] developed an HC-ARF-based Raman gas sensing system capable of highly sensitive and simultaneous multi-component detection of key gases generated during thermal runaway of lithium-ion batteries. The system employs a 2-m-long HC-ARF coupled with a micro-mirror at its distal end and incorporates a dual noise-reduction strategy that combines region-of-interest (ROI) selection on the

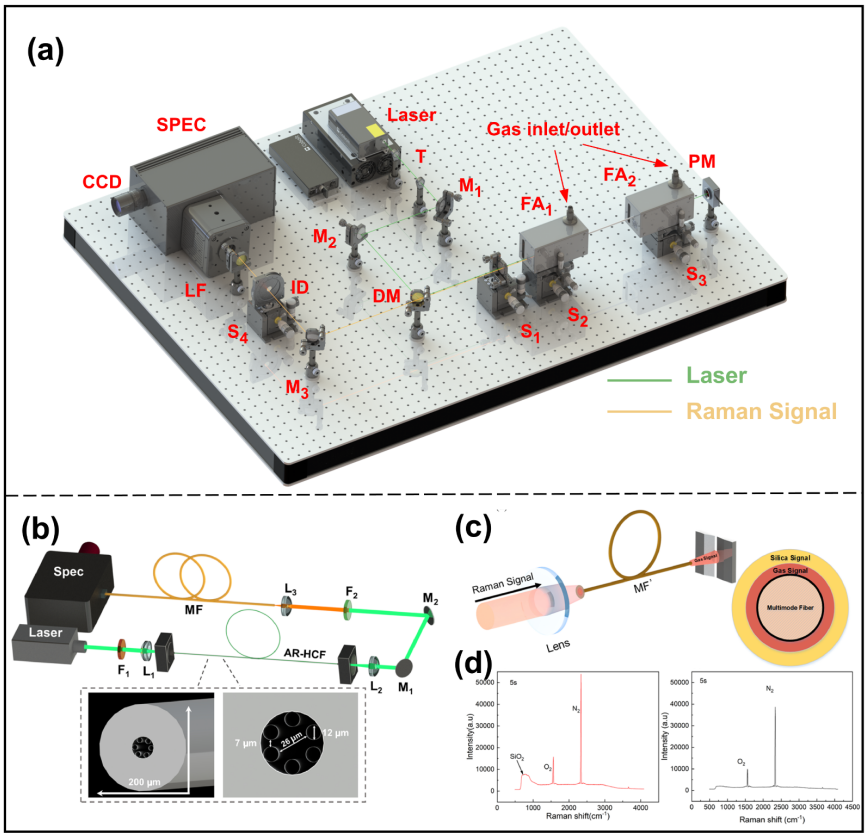


**Figure 12** HC-ARF-based FERS gas sensors. (a) FERS setup for detecting key gases generated during the thermal runaway of lithium-ion batteries (reproduced from Ref. [112]). (b–d) FERS sensor for $CO_2$ isotope detection [113]: (b) experimental setup (inset: 3D model and microscope image of the HC-ARF cross section); (c) schematic illustration of the spatial filtering process; (d) comparison of Raman signals (left) without and (right) with spatial filtering.

charge-coupled device (CCD) with an adjustable iris diaphragm (ID). This configuration substantially enhances both Raman signal intensity and the SNR. As shown in Figure 12a, the system achieved ppm-level detection limits for seven gases, $CH_4$, $C_2H_6$, $C_2H_4$, $C_2H_2$, CO, $CO_2$, and $H_2$, within a 60 s integration time (e.g., $CH_4$ as low as 0.8 ppm), providing an effective pathway for *in-situ* and non-destructive evaluation of battery health.

In contrast, recent work by Yang *et al*. [113] demonstrated the capability of FERS combined with HC-ARF for isotope-resolved gas sensing. To address the limited signal collection efficiency per unit length caused by the low numerical aperture of HC-ARF, the study adopted a forward-scattering optical configuration and extended the fiber length to 5 m (Figure 12b). Moreover, by exploiting the attenuation characteristics of the $SiO_2$ background signal during transmission and using a 10-μm-core-diameter MMF as a "fiber pinhole" for spatial filtering, the system effectively suppressed cladding-induced background interference and substantially reduced spectral baseline drift (Figure 12c, d). Under a laser power of 1.8 W and an integration time of 300 s, the system achieved detection limits of 0.5 ppm for $^{13}C^{16}O_2$ and 1.2 ppm for $^{12}C^{16}O_2$ in air, demonstrating the strong potential of HC-ARF-based FERS for trace-gas monitoring and isotope-tracing applications.

## Other detection methods

To explore the application potential of HC-ARFs in gas sensing, researchers have focused on integrating various spectroscopic detection techniques with HC-ARFs, such as chirped laser dispersion spectroscopy (CLaDS) [114], heterodyne phase-sensitive dispersion spectroscopy (HPSDS) [115], and light-induced thermoelastic spectroscopy (LITES) [116,117]. Compared with absorption spectroscopy, dispersion spectroscopy has attracted increasing attention due to its inherent advantages of immunity to laser power fluctuations, calibration-free operation, and a broader dynamic range [118]. This technique retrieves gas state parameters by probing the RI variation (i.e., dispersion) accompanying molecular absorption near resonance frequencies [119]. The CLaDS method detects instantaneous frequency shifts induced by RI steps when a chirped multi-frequency signal propagates through the gas sample [120,121]. Increasing the chirp sweep rate enhances the frequency-shift signal, thereby improving detection sensitivity. Because spectral information is encoded in the frequency or phase domain rather than the amplitude domain, CLaDS exhibits strong immunity to amplitude noise and power fluctuations [122]. When combined with HC-ARFs, CLaDS benefits from the long interaction path and low optical loss of the fiber, enabling compact, alignment-free, and highly sensitive sensing architectures [114]. However, as a frequency-domain technique, CLaDS requires an expensive spectrum analyzer for high-speed frequency acquisition and a high-bandwidth laser controller to handle rapid modulation. In contrast, HPSDS analyzes gas parameters by detecting the relative phase shift induced by gas dispersion in a triplet optical signal generated through high-frequency intensity modulation. It does not require a chirped laser source or high-end spectrum analyzer, offering a simpler optical layout that facilitates data acquisition (DAQ) and concentration retrieval [123,124]. When integrated with HC-ARFs, the efficient light confinement and reduced beam divergence significantly improve modulation stability and SNR. Nevertheless, since HPSDS typically operates with modulation frequencies in the 100 MHz–10 GHz range, it imposes stricter performance requirements on the modulator and detection electronics.

LITES, also known as quartz-enhanced photoacoustic spectroscopy (QEPAS), is a non-contact detection technique based on the thermoelastic effect of a QTF. It features low cost, small footprint, high sensitivity, and broadband spectral applicability [125]. When the modulated laser passes through the gas and illuminates the QTF surface, a portion of the optical energy is absorbed and converted into heat, which induces thermoelastic expansion and mechanical vibration of the QTF. Owing to its resonance characteristics, the QTF amplifies this vibration and, via the piezoelectric effect, converts it into an electrical signal corresponding to the target gas concentration [126]. The high sensitivity of LITES depends on the quality factor ($Q$-factor) of the QTF; thus, designing customized QTFs with higher $Q$-factors and lower resonance frequencies represents an effective approach to further enhance sensor performance [127]. The combination of LITES with HC-ARFs enables in-fiber, compact, and highly robust acoustic sensing, as the confined light-gas interaction region enhances photothermal conversion efficiency and mechanical response.

Overall, although these techniques differ in their operating principles, their integration with HC-ARFs offers synergistic advantages, including enhanced light-gas interaction, improved SNR, and miniaturized, alignment-free configurations, collectively contributing to greater stability and sensitivity in advanced gas sensing systems.

Table 1 summarizes key performance parameters of HC-ARF-based gas sensors employing different detection techniques reported in recent years. Current HC-ARF-based gas sensors are evolving toward

**Table 1** HC-ARF-based gas sensors employing different sensing technologies

| Methods | Gas | Laser wavelength (μm) | Integration time (s) | LoD (ppb) | NEA ($cm^{-1}$) | NNEA ($W\ cm^{-1}\ Hz^{-1/2}$) | Ref. |
|---|---|---|---|---|---|---|---|
| TDLAS | $C_2H_2$ | 10.500 | 80 | 10 | $4.0 \times 10^{-7}$ | | [42] |
| | $CO_2$ | 2.000 | 10 | 34300 | | | [128] |
| | CO | 2.300 | 100 | 220 | | | [129] |
| PTS | NO | 5.260 | 144 | 11 | | $4.29 \times 10^{-7}$ | [130] |
| | $CH_4$ | 1.651 | 450 | 24.2 | $7.43 \times 10^{-9}$ | | |
| | $C_2H_2$ | 1.532 | 450 | 11.6 | $1.35 \times 10^{-8}$ | | [131] |
| | $NH_3$ | 1.532 | 450 | 46.1 | $9.87 \times 10^{-9}$ | | |
| | $CH_4$ | 1.654 | 200 | 0.015 | $5.6 \times 10^{-12}$ | | |
| | $C_2H_2$ | 1.532 | 113 | 0.0027 | | | [132] |
| | $O_2$ | 0.761 | 70 | 560 | | | |
| | $H_2O$ | 1.390 | 1000 | 222 | $3.57 \times 10^{-9}$ | | |
| | $CO_2$ | 2.000 | 1000 | 1.5 | $2.33 \times 10^{-9}$ | | [133] |
| | CO | 4.600 | 1000 | 0.6 | | | |
| | CO | 4.602 | 600 | 35 | | | |
| | $CO_2$ | 2.004 | 280 | 120 | | | [134] |
| | $C_2H_4$ | 3.346 | 280 | 310 | | | |
| | $C_2H_6$ | 3.348 | 280 | 49 | | | |
| | $C_2H_2$ | 1.530 | 320 | 1 | $1 \times 10^{-9}$ | | [135] |
| PAS | $C_2H_2$ | 1.533 | 100 | 8 | $2.81 \times 10^{-8}$ | | [102] |
| FERS | $CH_4$ | 0.532 | 60 | 1200 | | | [136] |
| | $C_2H_4$ | | 60 | 1600 | | | |
| | $C_2H_2$ | | 60 | 2700 | | | |
| | $C_2H_6$ | | 60 | 2900 | | | |
| | $H_2$ | | 60 | 13800 | | | |
| | CO | | 60 | 16700 | | | |
| | $H_2$ | 0.532 | 30 | 11200 | | | [137] |
| | $C_2H_2$ | | 30 | 3100 | | | |
| | $CO_2$ | | 30 | 9400 | | | |
| | $C_2H_4$ | | 30 | 4800 | | | |
| | $CH_4$ | | 30 | 1500 | | | |
| | CO | | 30 | 17900 | | | |
| | $^{13}C^{16}O_2$ | 0.532 | 900 | 135 | | | [138] |
| | $^{12}C^{16}O_2$ | | 900 | 510 | | | |
| | $^{12}C^{16}O^{18}O$ | | 900 | 221 | | | |
| | $CH_4$ | | 900 | 98 | | | |
| | $^{13}CO_2$ | 0.532 | 300 | 70 | | | [139] |
| | $^{12}CO_2$ | | 300 | 640 | | | |
| CLaDS | $C_2H_6$ | 3.336 | 25 | 0.0155 | | $3.5 \times 10^{-10}$ | [113] |
| HPSDS | NO | 5.260 | 80 | 800 | | | [114] |
| | $CH_4$ | 1.654 | 1285 | 1220 | | | [140] |
| LITES | $CH_4$ | 1.651 | 100 | 220 | $8.23 \times 10^{-8}$ | $2.04 \times 10^{-11}$ | [141] |
| | $N_2O$ | 4.570 | 50 | 40 | $8.6 \times 10^{-7}$ | | [142] |
| | $CO_2$ | 2.006 | 100 | 20000 | $1.7 \times 10^{-6}$ | | |
| | CO | 2.330 | 100 | 3850 | | $1.15 \times 10^{-7}$ | [116] |
| | $C_2H_2$ | 1.530 | 100 | 1670 | | | [143] |

achieving lower detection limits, shorter response times, and multi-gas detection capabilities. Meanwhile, researchers continue to explore novel sensing mechanisms aimed at further reducing system noise and fully harnessing the application potential of HC-ARF-based gas sensors.

## SUMMARY AND PROSPECTS

HC-ARF-based gas sensors have achieved remarkable progress in recent years. As a promising alternative to conventional free-space optical gas sensors, they provide new opportunities for gas detection with outstanding sensitivity and long-term stability. Rationally designed HC-ARFs enable low-loss, single-mode transmission and can function as compact gas cells with extended optical path lengths. When combined with advanced laser spectroscopy techniques, these fibers exhibit robust and versatile gas detection capabilities. Such characteristics render HC-ARF-based sensors suitable for a wide range of practical applications, from cost-effective and miniaturized devices to high-precision trace-gas detection and remote, distributed multi-gas sensing. Moreover, they open new avenues for the development of detection methodologies, including TDLAS, PTS, PAS, and RS.

However, HC-ARF gas sensing technology still faces substantial challenges in practical implementation. Although sensor sensitivity theoretically increases with fiber length, actual performance is limited by factors such as laser power, fiber transmission losses, and gas exchange efficiency. While microchannel fabrication can greatly shorten gas diffusion time, it requires expensive equipment and involves complex, time-consuming processes that increase production costs and inevitably introduce additional optical losses. The use of chalcogenide glass extends the sensing range of HC-ARFs into the MIR region; however, its low mechanical strength and poor thermal viscosity make fiber drawing difficult, leading to higher propagation losses and restricted applicability. Conversely, integrating advanced spectral detection techniques such as HPSDS and LITES with HC-ARFs has significantly enhanced detection accuracy and noise immunity, effectively reducing the detection limit. Looking forward, breakthroughs in low-loss fiber fabrication, improvements in spectroscopic detection methodologies, and the exploration of novel sensing mechanisms are expected to substantially advance the practical deployment and overall performance of HC-ARF-based gas sensors.

In summary, with continued technological innovation and expanding application domains, HC-ARF gas sensing technology is poised to become a major branch in the field of gas detection, making significant contributions to healthcare diagnostics, environmental monitoring, and industrial process control.

## Funding

This work was financially supported by the National Natural Science Foundation of China (62475201) and the Fundamental Research Funds for the Central Universities (104972024JYS0045).

## Conflict of interest

The authors declare no conflict of interest.

## References

1 Poletti F, Wheeler NV, Petrovich MN, *et al.* Towards high-capacity fibre-optic communications at the speed of light in

vacuum. *Nat Photon* 2013; **7**: 279–284.

2 Jaworski P, Kozioł P, Krzempek K, *et al.* Antiresonant hollow-core fiber-based dual gas sensor for detection of methane and carbon dioxide in the near- and mid-infrared regions. *Sensors* 2020; **20**: 3813.

3 Kornaszewski LW, Gayraud N, Stone JM, *et al.* Mid-infrared methane detection in a photonic bandgap fiber using a broadband optical parametric oscillator. *Opt Express* 2007; **15**: 11219–11224.

4 Miao R, Zhang X, Zhang J, *et al.* Hollow-core anti-resonant optical fibers for chemical and biomedical sensing. *Sens Bio-Sens Res* 2024; **46**: 100701.

5 Yu S, Zhang Z, Xia H, *et al.* Photon-counting distributed free-space spectroscopy. *Light Sci Appl* 2021; **10**: 212.

6 Nikodem M, Gomółka G, Klimczak M, *et al.* Laser absorption spectroscopy at 2 μm inside revolver-type anti-resonant hollow core fiber. *Opt Express* 2019; **27**: 14998–15006.

7 Hu J, Menyuk CR. Understanding leaky modes: Slab waveguide revisited. *Adv Opt Photon* 2009; **1**: 58–106.

8 Lai CH, Sun CK, Chang H. Terahertz antiresonant-reflecting-hollow-waveguide-based directional coupler operating at antiresonant frequencies. *Opt Lett* 2011; **36**: 3590–3592.

9 Litchinitser NM, Abeeluck AK, Headley C, *et al.* Antiresonant reflecting photonic crystal optical waveguides. *Opt Lett* 2002; **27**: 1592–1594.

10 Chang Y, Zhang H, Xu Y, *et al.* Low-loss nodeless hollow-core anti-resonant soft glass fiber for the 4 μm mid-infrared spectral range. *Opt Express* 2024; **32**: 23712–23721.

11 Chen X, Hu X, Yang L, *et al.* Double negative curvature anti-resonance hollow core fiber. *Opt Express* 2019; **27**: 19548–19554.

12 Hoo YL, Jin W, Shi C, *et al.* Design and modeling of a photonic crystal fiber gas sensor. *Appl Opt* 2003; **42**: 3509–3515.

13 Hodgkinson J, Tatam RP. Optical gas sensing: A review. *Meas Sci Technol* 2013; **24**: 012004.

14 Benabid F, Knight JC, Antonopoulos G, *et al.* Stimulated Raman scattering in hydrogen-filled hollow-core photonic crystal fiber. *Science* 2002; **298**: 399–402.

15 Wang YY, Wheeler NV, Couny F, *et al.* Low loss broadband transmission in hypocycloid-core Kagome hollow-core photonic crystal fiber. *Opt Lett* 2011; **36**: 669–671.

16 Wang YY, Peng X, Alharbi M, *et al.* Design and fabrication of hollow-core photonic crystal fibers for high-power ultrashort pulse transportation and pulse compression. *Opt Lett* 2012; **37**: 3111–3113.

17 Yu F, Wadsworth WJ, Knight JC. Low loss silica hollow core fibers for 3–4 μm spectral region. *Opt Express* 2012; **20**: 11153–11158.

18 Kolyadin AN, Kosolapov AF, Pryamikov AD, *et al.* Light transmission in negative curvature hollow core fiber in extremely high material loss region. *Opt Express* 2013; **21**: 9514–9519.

19 Gao S, Wang Y, Ding W, *et al.* Hollow-core conjoined-tube negative-curvature fibre with ultralow loss. *Nat Commun* 2018; **9**: 2828.

20 Habib MS, Antonio-Lopez JE, Markos C, *et al.* Single-mode, low loss hollow-core anti-resonant fiber designs. *Opt Express* 2019; **27**: 3824–3836.

21 Nikodem M, Gomółka G, Klimczak M, *et al.* Demonstration of mid-infrared gas sensing using an anti-resonant hollow core fiber and a quantum cascade laser. *Opt Express* 2019; **27**: 36350–36357.

22 Zheng W, Qin Y, Xu O, *et al.* Wideband low confinement loss anti-resonant hollow core fiber with nested U-shape tube. *Opt Express* 2021; **29**: 24182–24192.

23 Zhang X, Song W, Dong Z, *et al.* Low loss nested hollow-core anti-resonant fiber at 2 μm spectral range. *Opt Lett* 2022; **47**: 589–592.

24 Wu D, Yu F, Wu C, *et al.* Low-loss multi-mode anti-resonant hollow-core fibers. *Opt Express* 2023; **31**: 21870–21880.

25 Hong YF, Jia AQ, Gao SF, *et al.* Birefringent, low loss, and broadband semi-tube anti-resonant hollow-core fiber. *Opt*

*Lett* 2023; **48**: 163–166.

26 Gao S, Chen H, Sun Y, *et al.* Truncated anti-resonant hollow-core fiber for reduced microstructure diameter. *J Lightwave Technol* 2024; **42**: 6077–6082.

27 Hao Y, Guo H, Wang P, *et al.* Ultra-low loss bending resistant few-mode hollow core anti-resonant fiber with nested elliptical tubes. *Opt Laser Tech* 2025; **186**: 112685.

28 Petrovich M, Numkam Fokoua E, Chen Y, *et al.* Broadband optical fibre with an attenuation lower than 0.1 decibel per kilometre. *Nat Photon* 2025; **19**: 1203–1208.

29 Xu H, Yang Y, Yuan J, *et al.* Low loss and high polarization-maintaining single-mode hollow-core anti-resonant fibers with S+C+L+U communication bands. *Photonics* 2025; **12**: 846.

30 Belardi W, Pastre A, Bigot L, et al. Silica based optical fibers with record attenuation in the mid-infrared. In: *Proceedings of the Programs and Abstracts of Optical Fabrication and Testing 2023*. Québec, 2023.

31 Arman H, Olyaee S, Seifouri M. Numerical optimization of anti resonant hollow core fiber for high sensitivity methane detection. *Sci Rep* 2024; **14**: 31534.

32 Yu F, Knight JC. Spectral attenuation limits of silica hollow core negative curvature fiber. *Opt Express* 2013; **21**: 21466–21471.

33 Zhu J, Feng S, Liu C, *et al.* Design and fabrication of a tellurite hollow-core anti-resonant fiber for mid-infrared applications. *Opt Express* 2024; **32**: 14067–14077.

34 Zhu J, Liu C, Zhang Z, *et al.* Low-loss tellurite anti-resonant hollow-core fiber for 2–10 μm laser delivery. *Opt Lett* 2025; **50**: 5909–5912.

35 Yao C, Hu M, Ventura A, *et al.* Tellurite hollow-core antiresonant fiber-coupled quantum cascade laser absorption spectroscopy. *J Lightwave Technol* 2021; **39**: 5662–5668.

36 He L, Liang Y, Guan Y, *et al.* Large mode-area all-solid anti-resonant fiber based on chalcogenide glass for mid-infrared transmission. *Opt Express* 2023; **31**: 8975–8986.

37 Zhang H, Chang Y, Xu Y, *et al.* Design and fabrication of a chalcogenide hollow-core anti-resonant fiber for mid-infrared applications. *Opt Express* 2023; **31**: 7659–7670.

38 Jewell JM, Aggarwal ID. Determination of intrinsic mid-infrared absorption of a fluoride glass. *Opt Lett* 1991; **16**: 1554–1556.

39 Ren H, Wu D, Qiu T, *et al.* Low-loss chalcogenide anti-resonant hollow-core fiber for mid-infrared power delivery at wavelengths beyond 8 μm. *Optical Mater* 2025; **162**: 116844.

40 Gattass RR, Rhonehouse D, Gibson D, *et al.* Infrared glass-based negative-curvature anti-resonant fibers fabricated through extrusion. *Opt Express* 2016; **24**: 25697–25703.

41 Hayashi JG, Ventura A, Cimek J, et al. Extruded antiresonant hollow core fibers for mid-IR Laser delivery. In: *Proceedings of the 22nd International Conference on Transparent Optical Networks (ICTON 2020)*. Bari, 2020, 1−4..

42 Hu M, Ventura A, Grigoleto Hayashi J, *et al.* Mid-infrared absorption spectroscopy of ethylene at 10.5 μm using a chalcogenide hollow-core antiresonant fiber. *Opt Laser Tech* 2023; **158**: 108932.

43 Zhang H, Chang Y, Xu Y, *et al.* Analytical investigation of total losses in anti-resonant hollow-core fibers comprising different materials at mid-infrared wavelengths. *Phys Scr* 2025; **100**: 105502.

44 Wang F, Yuan W, Hansen O, *et al.* Selective filling of photonic crystal fibers using focused ion beam milled microchannels. *Opt Express* 2011; **19**: 17585–17590.

45 Martelli C, Olivero P, Canning J, *et al.* Micromachining structured optical fibers using focused ion beam milling. *Opt Lett* 2007; **32**: 1575–1577.

46 Jason K, William C, Matthias K, et al. Fugitive methane leak detection using mid-infrared hollow-core photonic crystal fiber containing ultrafast laser drilled side-holes. In: *Proceedings of Fiber Optic Sensors and Applications XIII*. Baltimore, 2016, 985210.

47 Hensley C, Broaddus DH, Schaffer CB, *et al.* Photonic band-gap fiber gas cell fabricated using femtosecond micromachining. *Opt Express* 2007; **15**: 6690–6695.

48 Kozioł P, Jaworski P, Krzempek K, *et al.* Fabrication of microchannels in a nodeless antiresonant hollow-core fiber using femtosecond laser pulses. *Sensors* 2021; **21**: 7591.

49 Kozioł P, Bojęś P, Jaworski P, *et al.* Enhancing gas diffusion in antiresonant hollow-core fiber gas sensors using microchannels. *Photonic Sens* 2025; **15**: 250336.

50 Liu C, Tao W, Chen C, *et al.* Fabricating air pressure sensors in hollow-core fiber using femtosecond laser pulse. *Micromachines* 2022; **14**: 101.

51 Zhao P, Zhao Y, Bao H, *et al.* Mode-phase-difference photothermal spectroscopy for gas detection with an anti-resonant hollow-core optical fiber. *Nat Commun* 2020; **11**: 847.

52 Warrington EA, Peverall R, Salter PS, et al. A high sensitivity, fast response optical fiber gas sensor using micro-drilled anti-resonant fiber. In: *Proceedings of the 28th International Conference on Optical Fiber Sensors (OFS-28)*, *Technical Digest Series*. Naka-ku, Hamamatsu-shi, 2023.

53 Krzempek K. Part-per-billion level photothermal nitric oxide detection at 5.26 μm using antiresonant hollow-core fiber-based heterodyne interferometry. *Opt Express* 2021; **29**: 32568–32579.

54 Novo CC, Choudhury D, Siwicki B, *et al.* Femtosecond laser machining of hollow-core negative curvature fibres. *Opt Express* 2020; **28**: 25491–25501.

55 Wang J, Chen W, Wang P, *et al.* Fiber-enhanced Raman spectroscopy for highly sensitive $H_2$ and $SO_2$ sensing with a hollow-core anti-resonant fiber. *Opt Express* 2021; **29**: 32296–32311.

56 Warrington EA, Salter PS, Davis WOC, *et al.* Micro-drilling hollow-core fiber using image processing for rotational alignment. *Opt Express* 2025; **33**: 23616–23631.

57 Zhang JY, Ding EJ, Xu SC, *et al.* Sensitization of an optical fiber methane sensor with graphene. *Opt Fiber Tech* 2017; **37**: 26–29.

58 Yu C, Wu Y, Liu X, *et al.* Miniature fiber-optic $NH_3$ gas sensor based on Pt nanoparticle-incorporated graphene oxide. *Sens Actuat B-Chem* 2017; **244**: 107–113.

59 Sangeetha M, Madhan D. Ultra sensitive molybdenum disulfide ($MoS_2$)/graphene based hybrid sensor for the detection of $NO_2$ and formaldehyde gases by fiber optic clad modified method. *Opt Laser Tech* 2020; **127**: 106193.

60 Wang T, Zhu L, Yue Y, *et al.* Fiber-optic sensor modified by electrospun polymer/$Ti_3C_2$ MXene-$TiO_2$ for dimethyl sulfoxide sensing. *Talanta* 2025; **287**: 127630.

61 Sun D, Xu S, Liu S, *et al.* A fiber-optic ultraviolet sensor based on the evanescent field: Enhanced effects of black phosphorous film. *Opt Fiber Tech* 2021; **67**: 102747.

62 Yang J, Zhou L, Che X, *et al.* Photonic crystal fiber methane sensor based on modal interference with an ultraviolet curable fluoro-siloxane nano-film incorporating cryptophane A. *Sens Actuat B-Chem* 2016; **235**: 717–722.

63 Liu H, Wang H, Chen C, *et al.* High sensitive methane sensor based on twin-core photonic crystal fiber with compound film-coated side-holes. *Opt Quant Electron* 2020; **52**: 81.

64 Giovanardi F, Cucinotta A, Rozzi A, *et al.* Hollow core inhibited coupling fibers for biological optical sensing. *J Lightwave Technol* 2019; **37**: 2598–2604.

65 Ermatov T, Noskov RE, Machnev AA, *et al.* Multispectral sensing of biological liquids with hollow-core microstructured optical fibres. *Light Sci Appl* 2020; **9**: 173.

66 Xia Z, Zhang X, Yao J, *et al.* Giant enhancement of raman scattering by a hollow-core microstructured optical fiber allows single exosome probing. *ACS Sens* 2023; **8**: 1799–1809.

67 Liu W, Zheng Y, Wang Z, *et al.* Ultrasensitive exhaled breath sensors based on anti-resonant hollow core fiber with *in situ* grown ZnO-$Bi_2O_3$ nanosheets. *Adv Mater Inter* 2021; **8**: 2001978.

68 Maurya P, Kushwaha A, Verma R. High performance SPR gas sensor by using heterostructure of 2D materials

graphene/black phosphorous/$MoS_2$. *Sens Imag* 2024; **25**: 66.

69 Li Y, Chen H, Chen Q, *et al.* Surface plasmon resonance induced methane gas sensor in hollow core anti-resonant fiber. *Opt Fiber Tech* 2023; **78**: 103293.

70 Itoh T, Procházka M, Dong ZC, *et al.* Toward a new era of SERS and TERS at the nanometer scale: From fundamentals to innovative applications. *Chem Rev* 2023; **123**: 1552–1634.

71 Lei T, Deng C, Yang X, *et al.* Surface-enhanced Raman scattering optical fiber sensors: Advances and prospects. *J Raman Spectr* 2025; jrs.70058.

72 Ding H, Hu DJJ, Yu X, *et al.* Review on all-fiber online Raman sensor with hollow core microstructured optical fiber. *Photonics* 2022; **9**: 134.

73 Wei J, Liu Y, Niu M, *et al.* Advances in fiber optic surface-enhanced raman spectroscopy sensors. *ACS Photon* 2025; **12**: 5312–5344.

74 Kolchanov D, Machnev A, Barhom H, et al. Gilded hollow-core fibers for sensing and endoscopy. In: *Proceedings of the 2024 IEEE Opto-Electronics and Communications Conference (OECC 2024)*. Melbourne, 2024, 241.

75 Merdalimova AA, Rudakovskaya PG, Ermatov TI, *et al.* SERS platform based on hollow-core microstructured optical fiber: Technology of UV-mediated gold nanoparticle growth. *Biosensors* 2022; **12**: 19.

76 Gao W, Wang X, He Y, *et al.* Sub-ppm $NO_2$ gas sensing in CdTe quantum dots functionalized hollow-core anti-resonant fiber. *Sens Actuat B-Chem* 2024; **405**: 135350.

77 Benoy T, Wilson D, Lengden M, *et al.* Measurement of $CO_2$ concentration and temperature in an aero engine exhaust plume using wavelength modulation spectroscopy. *IEEE Sens J* 2017; **17**: 6409–6417.

78 Krzempek K. A review of photothermal detection techniques for gas sensing applications. *Appl Sci* 2019; **9**: 2826.

79 Schiff HI, Mackay GI, Bechara J. The use of tunable diode laser absorption spectroscopy for atmospheric measurements. *Res Chem Intermed* 1994; **20**: 525–556.

80 Fathy A, Sabry YM, Hunter IW, *et al.* Direct absorption and photoacoustic spectroscopy for gas sensing and analysis: A critical review. *Laser Photon Rev* 2022; **16**: 2100556.

81 Chai K, Hu B, Fu Z, *et al.* Tunable diode laser absorption spectroscopy for gas detection with a negative curvature anti-resonant hollow-core fiber. *Opt Commun* 2025; **575**: 131278.

82 Gomółka G, Stępniewski G, Pysz D, *et al.* Highly sensitive methane detection using a mid-infrared interband cascade laser and an anti-resonant hollow-core fiber. *Opt Express* 2023; **31**: 3685.

83 Goldenstein CS, Strand CL, Schultz IA, *et al.* Fitting of calibration-free scanned-wavelength-modulation spectroscopy spectra for determination of gas properties and absorption lineshapes. *Appl Opt* 2014; **53**: 356.

84 Gomółka G, Pysz D, Buczyński R, *et al.* Wavelength modulation spectroscopy of oxygen inside anti-resonant hollow-core fiber-based gas cell. *Opt Laser Tech* 2024; **170**: 110323.

85 Li C, Shao L, Meng H, *et al.* High-speed multi-pass tunable diode laser absorption spectrometer based on frequency-modulation spectroscopy. *Opt Express* 2018; **26**: 29330–29339.

86 Hu M, Ventura A, Hayashi JG, *et al.* Mid-infrared frequency modulation spectroscopy of no detection in a hollow-core antiresonant fiber. *Photonics* 2022; **9**: 935.

87 Nikodem M, Krzempek K, Dudzik G, *et al.* Hollow core fiber-assisted absorption spectroscopy of methane at 34 μm. *Opt Express* 2018; **26**: 21843.

88 Krzempek K, Abramski K, Nikodem M. Kagome hollow core fiber-based mid-infrared dispersion spectroscopy of methane at sub-ppm levels. *Sensors* 2019; **19**: 3352.

89 Piotr J. Molecular dispersion spectroscopy in a $CO_2$-filled all-fiber gas cells based on a hollow-core photonic crystal fiber. *Opt Eng* 2019; 58: 026112..

90 Bialkowski SE, Mandelis A. Photothermal spectroscopy methods for chemical analysis. *Phys Today* 1996; **49**: 76.

91 Krzempek K, Dudzik G, Abramski K. Photothermal spectroscopy of $CO_2$ in an intracavity mode-locked fiber laser

configuration. *Opt Express* 2018; **26**: 28861–28871.
92 Li Z, Wang Z, Yang F, *et al.* Mid-infrared fiber-optic photothermal interferometry. *Opt Lett* 2017; **42**: 3718.
93 Yao C, Wang Q, Lin Y, *et al.* Photothermal CO detection in a hollow-core negative curvature fiber. *Opt Lett* 2019; **44**: 4048–4051.
94 Yao C, Gao S, Wang Y, *et al.* Heterodyne interferometric photothermal spectroscopy for gas detection in a hollow-core fiber. *Sens Actuat B-Chem* 2021; **346**: 130528.
95 Wang Q, Wang Z, Zhang H, *et al.* Dual-comb photothermal spectroscopy. *Nat Commun* 2022; **13**: 2181.
96 Yao C, Shi Z, Li Z, *et al.* Fabry-Pérot photothermal interferometry in a hollow-core antiresonant fiber for gas detection in mid-infrared. *Sens Actuat B-Chem* 2024; **414**: 135930.
97 Jiang R, Yao C, Zhao X, *et al.* Highly sensitive photothermal gas detection enabled by a hollow-core antiresonant fiber with fiber Bragg gratings. *J Lightwave Technol* 2025; **43**: 2828–2834.
98 Yao C, Jiang S, Gao S, *et al.* Photothermal gas detection with a dithered low-finesse fiber-optic Fabry-Pérot interferometer. *J Lightwave Technol* 2023; **41**: 745–751.
99 Chen F, Jiang S, Jin W, *et al.* Ethane detection with mid-infrared hollow-core fiber photothermal spectroscopy. *Opt Express* 2020; **28**: 38115.
100 Hu M, Yao C, Hu M, *et al.* A comparative study of pump-probe photothermal spectroscopy using Mach-Zehnder interferometer and in-fiber mode interferometer. *Opt Lasers Eng* 2025; **185**: 108695.
101 Patimisco P, Scamarcio G, Tittel F, *et al.* Quartz-enhanced photoacoustic spectroscopy: A review. *Sensors* 2014; **14**: 6165–6206.
102 Zhao Y, Qi Y, Ho HL, *et al.* Photoacoustic Brillouin spectroscopy of gas-filled anti-resonant hollow-core optical fibers. *Optica* 2021; **8**: 532–538.
103 Xu Z, Li T, Sima C, *et al.* Mid-infrared hollow-core fiber based flexible longitudinal photoacoustic resonator for photoacoustic spectroscopy gas sensing. *Photonics* 2022; **9**: 895.
104 Zhang C, Antonio-Lopez JE, Amezcua-Correa R, *et al.* Photoacoustic methane detection assisted by a $H_2$-filled anti-resonant hollow-core fiber laser. *Opt Fiber Tech* 2025; **90**: 104126.
105 Zhang B, Shi Y. Design of flexible hollow core fiber based photoacoustic gas sensor with high cell constant and compact size. *Opt Express* 2023; **31**: 34708–34720.
106 Bischel WK, Black G. Wavelength dependence of Raman scattering cross sections from 200−600 nm. AIP Conf Proc 1983; 100: 181−187..
107 Wang P, Chen W, Wang J, *et al.* Hazardous gas detection by cavity-enhanced Raman spectroscopy for environmental safety monitoring. *Anal Chem* 2021; **93**: 15474–15481.
108 Wang XM, Li X, Liu WH, *et al.* Gas sensor based on surface enhanced Raman scattering. *Materials* 2021; **14**: 388.
109 Knebl A, Yan D, Popp J, *et al.* Fiber enhanced Raman gas spectroscopy. *TrAC Trends Anal Chem* 2018; **103**: 230–238.
110 Nie Q, Liu Z, Cheng M, *et al.* Review on hollow-core fiber based multi-gas sensing using Raman spectroscopy. *Photonic Sens* 2024; **14**: 240412.
111 Buric MP, Chen KP, Falk J, *et al.* Enhanced spontaneous Raman scattering and gas composition analysis using a photonic crystal fiber. *Appl Opt* 2008; **47**: 4255–4261.
112 Wan F, Liu Q, Kong WP, *et al.* High-sensitivity lithium-ion battery thermal runaway gas detection based on fiber-enhanced Raman spectroscopy. *IEEE Sens J* 2023; **23**: 6849–6856.
113 Yang M, Liu Z, Xiong L, *et al.* Antiresonant fiber-enhanced Raman spectroscopy gas sensing with 1 ppm sensitivity. *Opt Express* 2024; **32**: 4093–4101.
114 Jaworski P, Krzempek K, Bojęś P, *et al.* Mid-IR antiresonant hollow-core fiber based chirped laser dispersion spectroscopy of ethane with parts per trillion sensitivity. *Opt Laser Tech* 2022; **156**: 108539.
115 Hu M, Ventura A, Hayashi JG, *et al.* Trace gas detection in a hollow-core antiresonant fiber with heterodyne phase-

sensitive dispersion spectroscopy. *Sens Actuat B-Chem* 2022; **363**: 131774.

116 Ma Y, Feng W, Qiao S, *et al.* Hollow-core anti-resonant fiber based light-induced thermoelastic spectroscopy for gas sensing. *Opt Express* 2022; **30**: 18836–18844.

117 Chen W, Qiao S, He Y, *et al.* Mid-infrared all-fiber light-induced thermoelastic spectroscopy sensor based on hollow-core anti-resonant fiber. *Photoacoustics* 2024; **36**: 100594.

118 Martín-Mateos P, Hayden J, Acedo P, *et al.* Heterodyne phase-sensitive dispersion spectroscopy in the mid-infrared with a quantum cascade laser. *Anal Chem* 2017; **89**: 5916–5922.

119 Wang G, Wang R, Zhao W. Precise temperature measurement through wavelength modulation heterodyne phase-sensitive dispersion spectroscopy. *Photonics* 2025; **12**: 537.

120 Wysocki G, Weidmann D. Molecular dispersion spectroscopy for chemical sensing using chirped mid-infrared quantum cascade laser. *Opt Express* 2010; **18**: 26123–26140.

121 Pedro MM, Jakob H, Pablo A, et al. Quantum-cascade-laser-based heterodyne phase-sensitive dispersion spectroscopy in the mid-IR range: Capabilities and limitations. In: *Proceedings of Photonic Instrumentation Engineering IV (Proc. SPIE Vol. 10110)*. Bellingham: SPIE, 2017.

122 Nikodem M, Plant G, Sonnenfroh D, *et al.* Open-path sensor for atmospheric methane based on chirped laser dispersion spectroscopy. *Appl Phys B* 2015; **119**: 3–9.

123 Bonilla-Manrique OE, Moreno-Oyervides A, Mánguez-Martín R, *et al*. Direct high-frequency modulation of a quantum cascade laser for high-sensitivity molecular dispersion spectroscopy at ambient pressure. IEEE Trans Instrum Meas 2024; 73: 1−6..

124 Martín-Mateos P, Acedo P. Heterodyne phase-sensitive detection for calibration-free molecular dispersion spectroscopy. *Opt Express* 2014; **22**: 15143.

125 Hu Y, Qiao S, He Y, *et al.* Quartz-enhanced photoacoustic-photothermal spectroscopy for trace gas sensing. *Opt Express* 2021; **29**: 5121–5127.

126 Ma Y, He Y, Tong Y, *et al.* Quartz-tuning-fork enhanced photothermal spectroscopy for ultra-high sensitive trace gas detection. *Opt Express* 2018; **26**: 32103–32110.

127 Ma Y, He Y, Patimisco P, *et al.* Ultra-high sensitive trace gas detection based on light-induced thermoelastic spectroscopy and a custom quartz tuning fork. *Appl Phys Lett* 2020; **116**: 011103.

128 Chai K, Zheng Y, Hu B, *et al.* All-fiber pressure-adaptive $CO_2$ concentration monitoring based on negative curvature anti-resonance hollow core fiber. *Infrared Phys Tech* 2025; **148**: 105879.

129 Chai K, Zheng Y, Hu B, *et al.* Highly time-resolved all-fiber sensor for real-time carbon monoxide detection and microleakage diagnosis. *IEEE Sens J* 2025; **25**: 13005–13011.

130 Krzempek K, Jaworski P, Kozioł P, *et al.* Antiresonant hollow core fiber-assisted photothermal spectroscopy of nitric oxide at 5.26 μm with parts-per-billion sensitivity. *Sens Actuat B-Chem* 2021; **345**: 130374.

131 Liu F, Bao H, Ho HL, *et al.* Multicomponent trace gas detection with hollow-core fiber photothermal interferometry and time-division multiplexing. *Opt Express* 2021; **29**: 43445–43453.

132 Bao H, Jin W, Hong Y, *et al.* Phase-modulation-amplifying hollow-core fiber photothermal interferometry for ultrasensitive gas sensing. *J Lightwave Technol* 2022; **40**: 313–322.

133 Chen F, Jiang S, Ho HL, *et al.* Frequency-division-multiplexed multicomponent gas sensing with photothermal spectroscopy and a single NIR/MIR fiber-optic gas cell. *Anal Chem* 2022; **94**: 13473–13480.

134 Zheng K, Bao H, Luo W, *et al.* Hollow-core fiber-based mid-infrared photothermal spectroscopy for multi-component gas sensing. *IEEE J Sel Top Quantum Electron* 2024; **30**: 1–6.

135 Wu J, Zhao P, Bao H, *et al.* Hollow-core fiber fabry-pérot photothermal gas sensor: Temperature-dependent behavior. *J Lightwave Technol* 2025; **43**: 9458–9464.

136 Bai Y, Xiong D, Yao Z, *et al.* Analysis of $CH_4$, $C_2H_6$, $C_2H_4$, $C_2H_2$, $H_2$, CO, and $H_2S$ by forward Raman scattering with

a hollow-core anti-resonant fiber. *J Raman Spectr* 2022; **53**: 1023–1031.

137 Wan F, Kong W, Liu Q, *et al.* Fluorescence noise eliminating fiber-enhanced Raman spectroscopy for simultaneous and multiprocess analysis of intermediate compositions for $C_2H_2$ and $H_2$ production. *Anal Chem* 2023; **95**: 8596–8604.

138 Pei S, Nie Q, Liu Z, *et al.* Atmospheric environment monitoring by antiresonant fiber-enhanced Raman spectroscopy with sub-ppm sensitivity. *IEEE Sens J* 2024; **24**: 34604–34610.

139 Wan Y, Li X, Wang Z, *et al.* Trace gas detection using anti-resonant hollow-core fiber Raman spectroscopy based on a multi-stage spatial filtering method. *Opt Lasers Eng* 2025; **195**: 109341.

140 Zhang H, Wu T, Wu Q, *et al.* Methane detection with a near-infrared heterodyne phase-sensitive dispersion spectrometer at a stronger frequency modulation using direct injection-current dithering. *Opt Express* 2023; **31**: 25070–25081.

141 Bojęś P, Pokryszka P, Jaworski P, *et al.* Quartz-enhanced photothermal spectroscopy-based methane detection in an anti-resonant hollow-core fiber. *Sensors* 2022; **22**: 5504.

142 Bojęś P, Jaworski P, Pokryszka P, *et al.* Dual-band light-induced thermoelastic spectroscopy utilizing an antiresonant hollow-core fiber-based gas absorption cell. *Appl Phys B* 2023; **129**: 177.

143 Sun X, Chen W, He Y, *et al.* All-fiber LITES sensor based on hollow-core anti-resonant fiber and self-designed low-frequency quartz tuning fork. *Sensors* 2025; **25**: 2933.